SIAM J. SCI. COMPUT.
Vol. 0, No. 0, pp. 000–000

AN ENERGY STABLE C^0 FINITE ELEMENT SCHEME FOR A PHASE-FIELD MODEL OF VESICLE MOTION AND DEFORMATION*

LINGYUE SHEN†, ZHILIANG XU‡, PING LIN†, HUAXIONG HUANG§, AND SHIXIN XU¶

Abstract. A thermodynamically consistent phase-field model is introduced for simulating motion and shape transformation of vesicles under flow conditions. In particular, a general slip boundary condition is used to describe the interaction between vesicles and the wall of the fluid domain in the absence of cell-wall adhesion introduced by ligand-receptor binding. A second-order accurate in both space and time C^0 finite element method is proposed to solve the model governing equations. Various numerical tests confirm the convergence, energy stability, and conservation of mass and surface area of cells of the proposed scheme. Vesicles with different mechanical properties are also used to explain the pathological risk for patients with sickle cell disease.

Key words. vesicle, local inextensibility, energy stable scheme, narrow channel

AMS subject classifications. 65Z05, 76T99, 65M60, 92B05

DOI. 10.1137/21M1416631

1. Introduction.

Studying dynamic motion and shape transformation of biological cells is always a point of interest in cell biology because the shapes of the cells usually relate to their function. For example, many blood-related diseases are known to be associated with alterations in the geometry and membrane properties of red blood cells [56]. Red blood cells in diabetes or sepsis patients exhibit impaired cell deformability [17, 42]. During blood clot formation, an indicator of platelet activation is its shape change by forming filopodia and lamellipodia. Notably, platelets' shape changes facilitate their adhesion to the site of vascular injury and cohesion with other platelets or erythrocytes [54, 2].

In simulation study, it is vitally important to establish a proper model of cell membranes for analyzing the dynamical shape transformation of cells in addition to modeling intracellular and extracellular fluids. Various mathematical models were introduced for predicting cell morphology and function. Dissipative particle dynamics [33] models of red blood cell were developed in [41, 33, 40] and were used to study effects of red blood cells on platelet aggregation [41]. Models based on interface tracking or capturing such as level set method [60, 61, 50] were also developed [6, 29, 25, 24] to take into consideration the fluid-cell-structure interaction. In numerical treatment, various methods such as the immersed boundary method [30, 52, 39, 57, 59], immersed

*Submitted to the journal's Computational Methods in Science and Engineering section April 30, 2021; accepted for publication (in revised form) September 21, 2021; published electronically DATE. https://doi.org/10.1137/21M1416631

Funding: This work was supported by NSFC through grants 12071190, 11771040, 11861131004, and 91430106, by NSF through grants CDS&E-MSS 1854779 and NSF-1821242, and by NSERC.

†Department of Mathematics University of Dundee, Dundee DD1 4HN, UK (l.shen@dundee.ac.uk, P.Lin@dundee.ac.uk).

‡Department of Applied and Computational Mathematics and Statistics, University of Notre Dame, 102G Crowley Hall, Notre Dame, IN 46556 USA (zxu2@nd.edu).

§Research Centre for Mathematics, Advanced Institute of Natural Sciences, Beijing Normal University (Zhuhai), China; BNU- HKBU United International College, Zhuhai, China (hhuang@uic.edu.cn).

¶Duke Kunshan University, 8 Kunshan Street, Kunshan, Jiangsu, China (shixin.xu@dukekunshan.edu.cn).

interface method [26, 31], spectral method [34], and fictitious domain method [24] using finite difference or finite element formulation have been introduced to solve governing equations of these models.

The phase-field method considers the material interface as a diffuse layer instead of a sharp discontinuity. This regularization can be rigorously formulated through a variational process. The main advantages of the phase-field method are twofold. The phase-field order parameter identifying the diffuse interface is treated as an additional primary unknown of the problem to be solved on the whole domain. Consequently, interface transformations are predicted without the necessity of a remeshing algorithm to treat the evolution of the interface. The physics mediating the interface dynamics can be easily incorporated into the phase-field models.

Lots of phase-field–type vesicle models have been introduced lately [27, 65, 35, 11]. Mechanical properties of the vesicle membrane such as bending stiffness and inextensibility can be incorporated rigorously by the phase-field theory [11, 13, 14, 12] to establish a realistic mechanistic model. For instance, the bending energy of bending resistance of the lipid bilayer membrane in the isotropic case (neglecting the proteins and channels on the membrane) given in the form of the Helfrich bending energy can be approximated by a modified elastic energy defined on the whole domain in the phase-field formulation [8, 10, 13, 14]. Constraints conserving cell mass and ensuring global inextensibility of cell membrane are frequently introduced into vesicle models to keep the mass and surface area of the vesicle constant [12, 1].

The focus of this paper is to model flowing vesicles interacting with the domain boundaries which mimics scenarios such as red blood cells passing through a narrowed blood vessel in the absence of the cell-wall adhesion introduced by ligand-receptor binding or when the impact of this cell-wall adhesion can be neglected. This involves considering a moving contact line problem since three different phases meet to form a triple point [44]. The first goal of this paper thus is to derive a thermodynamically consistent phase-field model for vesicles' motion and shape transformation in a closed spatial domain by using an energy variational method [53, 21]. All the physics taken into consideration are introduced through definitions of energy functionals and dissipation functional, together with the kinematic assumptions of laws of conservation. Besides the energy and dissipation terms defined on bulk region of the domain, terms accounting for boundary effects are also added to the functionals. Then performing variation of these functionals yields an Allen–Cahn–Navier–Stokes system [58] with Allen–Cahn general Navier boundary conditions (GNBCs) [45]. This is in contrast to most previous works [13, 14, 7] in which a dynamic boundary condition was rarely derived during the course of model derivation. Dirichlet- or Neumann-type conditions were simply added to these models at the end to close the governing equations [1, 12, 10]. Moreover, in our model derivation, the incompressibility of the fluid, the local and global inextensibility of the vesicle membrane, and the conservation of vesicle mass are taken into account by introducing two Lagrangian multipliers, hydrostatic pressure and surface pressure [39] and penalty terms, respectively.

The second goal of this paper is to propose an efficient and accurate numerical scheme for solving the obtained fourth-order nonlinear coupled partial differential equation system. Over the past decades, a lot of schemes have been developed for Allen–Cahn– or Cahn–Hilliard–Navier–Stokes systems. As for systems such as vesicle models introduced in the current and other works which are more sophisticated than the Allen–Cahn– or Cahn–Hilliard–Navier–Stokes systems, the backward Euler time discretization method is frequently used [1, 13, 19, 18] leading to a first-order accurate scheme. Later on, decoupled energy stable schemes were proposed by Chen et al.

[7] and Francisco and Giordano [20] by introducing explicit, convective velocities. Liu, Song, and Xu [34] introduce a variational framework for an inextensible membrane with immerse boundary formula and propose a spectral method for solving the obtained problem. In the current work, an efficient, energy-law preserving (thus energy stable) and second-order accurate C^0 finite element scheme is proposed to solve the obtained vesicle system using ideas introduced in [22]. The key idea of this scheme is to utilize the midpoint method in time discretization to ensure the accuracy in time and that the form of the discrete energy dissipation law is the same as that of the continuous model. In order to properly treat the term related to inextensibility of the membrane, a relaxation term of local inextensibility as in [1] is introduced. The numerical study of convergence confirms the proposed scheme is second-order convergent in both time and space. Furthermore, vesicle deformation simulations illustrate that it is energy stable and numerically conserves mass and surface area of vesicles.

The introduction of the GNBC in this work makes it possible to study a broad class of complicated fluid-structure interaction problems. In this paper, the developed model is applied to studying vesicles passing through narrow channels. The results confirm that the more rounded the vesicles (smaller surface-volume ratio) are, the more likely the vesicles form a blockage when they pass through narrow channels. It is also worth noting that it is critical to include the local inextensibility of the vesicle membrane in the model when studying this type of problem. Without the local inextensibility, the vesicle membrane can be falsely stretched or compressed. Lastly, although membrane structures of vesicles and blood cells are quite different, a blood cell in many studies can be treated as an elastic capsule with bending rigidity, in which the membrane is impenetrable to both interior and exterior fluids. Therefore, our model developed for vesicles can be readily applied for studying a vast body of blood cell–related problems [37].

The rest of paper is organized as follows. Section 2 of the paper begins with introducing basic dynamical assumptions that have been used in many papers [12, 44] and is devoted to model derivation. Dimensionless model governing equations and the energy decaying law of the model are presented in section 3. In section 4, the numerical scheme solving the proposed model is developed, and its energy law is given. Numerical simulation results are described in section 5 to confirm the energy law of the numerical scheme and the feasibility of our model. A case study of a vesicle passing through a narrow channel is shown, which is to simulate the motion of red blood cells in a small blood vessel. Conclusions are drawn in section 6.

2. Model derivation. Derivation of the model for simulating a flowing vesicle deforming in a channel filled with extracellular fluid is presented in this section. The phase-field label function ϕ is introduced to track the motion of the vesicle, where $\phi(\boldsymbol{x}) = \pm 1$ denotes the intracellular and extracellular space and $\phi = 0$ is the vesicle membrane or interface.

The model is derived using an energy variational method [53]. It begins with defining two functionals for the total energy and dissipation of the system and introducing the kinematic equations based on physical laws of conservation. The specific forms of the flux and stress functions in the kinematic equations are obtained by taking the time derivative of the total energy functional and comparing with the defined dissipation functional. More details of this method can be found in [53].

In what follows, we detail steps of using this method to derive the model. We first make the following assumptions about mass and momentum conservation of the mixture of extracellular fluid and vesicle and interface inextensibility, and we assume that the dynamics of the phase-field function ϕ is an L^2 gradient flow:

$$\begin{cases} \dfrac{\partial \phi}{\partial t} + \nabla \cdot (\mathbf{u}\phi) = q_\phi \ , \\ \rho \left(\dfrac{\partial \mathbf{u}}{\partial t} + (\mathbf{u} \cdot \nabla)\mathbf{u} \right) = \nabla \cdot \boldsymbol{\sigma}_\eta + \mathbf{F}_\phi \ , \\ \nabla \cdot \mathbf{u} = 0 \ , \\ \delta_\gamma (\mathcal{P} : \nabla \mathbf{u}) + \ \xi \gamma^2 \nabla \cdot (\phi^2 \nabla \lambda) = 0 \end{cases} \tag{2.1}$$

with specific forms of flux q_ϕ, stress $\boldsymbol{\sigma}_\eta$, and body force density $\boldsymbol{F}_\phi$ functions to be determined. ρ and $\mathbf{u}$ are the density and velocity of the mixture, respectively. In this paper, we assume that the density is a constant. The first equation is the Allen–Cahn-type equation to track the interface. The second equation is the conservation of momentum. The third equation accounts for the fluid incompressibility (or mass conservation).

The last equation is related to the local inextensibility of the vesicle membrane. This local inextensibility prevents stretching on any point of the vesicle membrane surface [5]. In the sharp interface model, the local inextensibility (or mass conservation on the interface) is represented by $\nabla_\Gamma \cdot \mathbf{u} = 0$ defined on the interface Γ [35, 37]. This equation is equivalent to $\mathcal{P} : \nabla \mathbf{u} = 0$, where the projection operator $\mathcal{P}$ is defined to be $(I - \mathbf{n}_m \otimes \mathbf{n}_m)$ and $\mathbf{n}_m = \frac{\nabla \phi}{|\nabla \phi|}$ is the unit outward normal vector of the interface when it is defined as an implicit surface by the level function. In the phase-field formulation, the interface is modeled as a diffuse layer. This is different from the sharp interface concept. For computational convenience using phase-field formulation, this local inextensibility constraint on the interface Γ is extended to the domain Ω by multiplying with a scalar function

$$\delta_\gamma = \frac{1}{2}\gamma^2 |\nabla \phi|^2 \ , \tag{2.2}$$

where $\nabla \phi$ is nonzero only in the diffuse interface layer and γ is the thickness of the diffuse interface layer. Here a relaxation term $\xi \gamma^2 \nabla \cdot (\phi^2 \nabla \lambda)$ for the local inextensibility near the membrane is introduced as shown in [1]. ξ is a parameter independent of γ, and λ is the a function that measures the interface "pressure" induced by the inextensibility of the membrane.

On the wall boundary $\partial \Omega_w$ of the domain, the following boundary conditions are assumed:

$$\begin{cases} \mathbf{u} \cdot \mathbf{n} = 0 \ , \\ \mathbf{u}_\tau \cdot \boldsymbol{\tau}_i = f_{\tau_i} \ , \\ \dot{\phi} = \dfrac{\partial \phi}{\partial t} + \mathbf{u} \cdot \nabla_\Gamma \phi = J_\Gamma \ , \\ f = 0 \ , \\ \partial_n \lambda = 0 \ , \end{cases} \tag{2.3}$$

where an Allen–Cahn-type boundary condition is employed for ϕ, $\mathbf{u}_\tau = \mathbf{u} - (\mathbf{u} \cdot \mathbf{n})\mathbf{n}$ is the fluid slip velocity with respect to the wall, $\boldsymbol{\tau}_i, i = 1, 2$ are the tangential directions of the wall surface (2D), and $\nabla_\Gamma = \nabla - \mathbf{n}(\mathbf{n} \cdot \nabla)$ is the surface gradient operator on the boundary $\partial \Omega_w$. f_{τ_i} is the slip velocity of the fluid on the wall along the τ_i direction. And J_Γ represents the Allen–Cahn type of relaxation on the wall by using the phase-field method. Here we abuse the notation when there is no confusion, and the subscript Γ refers to $\partial \Omega_w$, and $\mathbf{n}$ is its unit outward normal. The meaning of equation $f = 0$ will be made explicit after definition of the interface curvature (see (2.8)).

The remainder of this section is devoted to deriving the exact forms of q_ϕ, $\boldsymbol{\sigma}_\eta$, $\mathbf{F}_\phi$, f_{τ_i}, and J_Γ using the energy variational method. By following the works in [58, 11], the total energy functional E_{total} of a cell- (or vesicle-) fluid system is defined to be the sum of the kinetic energy E_{kin}, the cell membrane energy E_{cell}, and the specific wall energy E_w due to the cell-wall interaction

$$E_{total} = \underbrace{E_{kin}}_{Macroscale} + \underbrace{E_{cell} + E_w}_{Microscale} . \tag{2.4}$$

The kinetic energy accounts for the transport of the cell-fluid mixture and is defined as

$$E_{kin} = \int_\Omega \left(\frac{1}{2} \rho |\mathbf{u}|^2 \right) d\boldsymbol{x} , \tag{2.5}$$

where ρ is the macroscale density of the mixture and is assumed to be equal to a constant ρ_0 in this work (matched density case).

The cell energy E_{cell} is defined to be the sum of the bending energy E_{bend} and two penalty terms in order to preserve the total volume and surface area of the cell:

$$E_{cell} = E_{bend} + \frac{M_v}{2} \frac{\left(V(\phi) - V(\phi_0)\right)^2}{V(\phi_0)} + \frac{M_s}{2} \frac{\left(S(\phi) - S(\phi_0)\right)^2}{S(\phi_0)} , \tag{2.6}$$

where $V(\phi) = \int_\Omega \phi d\boldsymbol{x}$ is the volume difference of the cell-fluid system and the value of $S(\phi) = \int_\Omega \frac{G(\phi)}{\gamma} d\boldsymbol{x}$ is used to measure the surface area of the cell with $G(\phi) = \int_\Omega \frac{\gamma^2 |\nabla \phi|^2}{2} + \frac{(1-\phi^2)^2}{4} d\boldsymbol{x}$. M_v and M_s are cell volume and surface area constraint coefficients, respectively.

If the cell membrane is assumed to be isotropic and only composed of a lipid bilayer, the bending energy of the bending resistance of the cell membrane can be modeled by an approximation of the Helfrich bending energy [11] as follows:

$$E_{bend} = \int_\Omega \frac{\hat{\kappa}_B}{2\gamma} \left| \frac{f(\phi)}{\gamma} \right|^2 d\boldsymbol{x} , \tag{2.7}$$

where $\hat{\kappa}_B$ is the bending modulus and

$$f(\phi) := \frac{\delta G}{\delta \phi} = -\gamma^2 \Delta \phi + (\phi^2 - 1)\phi . \tag{2.8}$$

In order to take into account the interaction at the interface between vesicle, fluid, and vessel wall on $\partial\Omega_w$, the wall free energy E_w is introduced:

$$E_w = \int_{\partial\Omega_w} f_w(\phi) ds , \tag{2.9}$$

where f_w is the vesicle-wall interaction energy density.

Remark 2.1. Here we borrow the idea introduced in moving contact line models [43, 44]:

$$f_w(\phi) = -\frac{\sigma}{2} \sin\left(\frac{\phi \pi}{2} \right) \cos(\theta_s) \tag{2.10}$$

with a static contact angle θ_s [48, 47] when the cell-wall adhesion is absent or negligible. This is justified by the fact that a triple point is formed at which wall, cell, and extracellular fluid meet, and its dynamics can be modeled through a contact line model. We also note that the choice of contact angle can be subtle and affects

simulation outcome. Low contact angle values show a tendency of the cell to spread and "adhere" to the surface (hydrophilic) due to the existence of a wetting force, whereas high contact angle values represent the surface's tendency to repel the cell or an absence of the wetting force (hydrophobic). (See Figure 4 in section 5.2 later.) In fact, the wall energy f_w can be made more sophisticated in order to faithfully represent the complicated vesicle-wall interaction in the case that the cell-wall adhesion by ligand-receptor binding is involved, for example, by introducing a new phase to represent the wall [18].

The chemical potential μ is obtained by taking the variation of $E_{bulk} = E_{kin}+E_{cell}$ with respect to ϕ:

$$\mu = \frac{\delta E_{bulk}}{\delta \phi} = \frac{\hat{\kappa}_B}{\gamma^3} g(\phi) + M_v \frac{V(\phi) - V(\phi_0)}{V(\phi_0)} + \frac{M_s}{\gamma} \frac{S(\phi) - S(\phi_0)}{S(\phi_0)} f(\phi) \ , \tag{2.11}$$

where $g(\phi) = -\gamma^2 \Delta f + (3\phi^2 - 1) f$.

It is assumed in the present work that dissipation of the system energy is due to fluid viscosity, friction on the wall, and interfacial mixing due to diffuse interface representation. Accordingly, the total dissipation functional Δ is defined as follows:

$$\begin{aligned} \Delta = & \int_\Omega 2\eta |\boldsymbol{D}_\eta|^2 d\boldsymbol{x} + \int_\Omega \frac{1}{M_\phi} |q_\phi|^2 d\boldsymbol{x} + \int_\Omega \xi |\gamma \phi \nabla \lambda|^2 d\boldsymbol{x} + \int_{\partial \Omega_w} \beta_s |\mathbf{u}_{\boldsymbol{\tau}}|^2 ds \\ & + \int_{\partial \Omega_w} \kappa_\Gamma |J_\Gamma|^2 ds \ . \end{aligned} \tag{2.12}$$

Here the first term is the macroscopic dissipation induced by the fluid viscosity with $\boldsymbol{D}_\eta = \frac{1}{2}[\nabla \mathbf{u} + (\nabla \mathbf{u})^T]$, the second term is the microscopic dissipation induced by the diffuse interface, the third term is the dissipation induced by the diffuse interface method for imposing local inextensibility of the interface, the fourth term is the boundary friction dissipation, where β_s is related to the roughness of the vessel wall, and the last term is the dissipation induced by the diffuse interface contacting the wall.

By taking the time derivative of the total energy functional (2.4), it is obtained that (detailed derivation is given in the appendix of this paper)

(2.13)

$$\begin{aligned} \frac{dE_{total}}{dt} &= \frac{d}{dt} E_{kin} + \frac{d}{dt} E_{cell} + \frac{d}{dt} E_w \\ &= -\int_\Omega ((\boldsymbol{\sigma}_\eta + pI) : \nabla \mathbf{u}) d\boldsymbol{x} + \int_\Omega (\mathbf{F}_\phi - \mu \nabla \phi - \nabla \cdot (\lambda \delta_\gamma \mathcal{P})) \cdot \mathbf{u} d\boldsymbol{x} + \int_\Omega \mu q_\phi d\boldsymbol{x} \\ &\quad + \int_\Omega \xi (\gamma \phi \nabla \lambda)^2 d\boldsymbol{x} + \int_{\partial \Omega_w} ((\boldsymbol{\sigma}_\eta + \lambda \delta_\gamma \mathcal{P}) \cdot \mathbf{n}) \cdot \mathbf{u}_\tau ds + \int_{\partial \Omega_s} \hat{L}(\phi) \frac{\partial \phi}{\partial t} ds \\ &= -\int_\Omega ((\boldsymbol{\sigma}_\eta + pI) : \nabla \mathbf{u}) d\boldsymbol{x} + \int_\Omega (\mathbf{F}_\phi - \mu \nabla \phi - \nabla \cdot (\lambda \delta_\gamma \mathcal{P})) \cdot \mathbf{u} d\boldsymbol{x} + \int_\Omega \mu q_\phi d\boldsymbol{x} \\ &\quad + \int_\Omega \xi (\gamma \phi \nabla \lambda)^2 d\boldsymbol{x} + \int_{\partial \Omega_w} ((\boldsymbol{\sigma}_\eta + \lambda \delta_\gamma \mathcal{P}) \cdot \mathbf{n}) \cdot \mathbf{u}_\tau ds + \int_{\partial \Omega_s} \hat{L}(\phi)(-\mathbf{u} \cdot \nabla_\Gamma \phi + J_\Gamma) ds \\ &= -\int_\Omega ((\boldsymbol{\sigma}_\eta + pI) : \nabla \mathbf{u}) d\boldsymbol{x} + \int_\Omega (\mathbf{F}_\phi - \mu \nabla \phi - \nabla \cdot (\lambda \delta_\gamma \mathcal{P})) \cdot \mathbf{u} d\boldsymbol{x} + \int_\Omega \mu q_\phi d\boldsymbol{x} \\ &\quad + \int_\Omega \xi (\gamma \phi \nabla \lambda)^2 d\boldsymbol{x} + \int_{\partial \Omega_w} ((\boldsymbol{\sigma}_\eta + \lambda \delta_\gamma \mathcal{P}) \cdot \mathbf{n} - \hat{L}(\phi) \nabla_\Gamma \phi) \cdot \mathbf{u}_\tau ds + \int_{\partial \Omega_w} \hat{L}(\phi) J_\Gamma ds, \end{aligned}$$

where p and λ are introduced as Lagrange multipliers accounting for fluid incompressibility and local inextensibility of the cell membrane, respectively. δ_γ is defined in (2.2), and $\hat{L}(\phi) = \frac{\hat{\kappa}_B}{\gamma} \partial_n f + M_s \frac{S(\phi) - S(\phi_0)}{S(\phi_0)} \gamma \partial_n \phi + \frac{\partial f_w}{\partial \phi}$.

Using the energy dissipation law $\frac{dE_{total}}{dt} = -\Delta$ [62, 15] and the definition of the dissipation functional (2.12), it is obtained that

$$\begin{cases} \boldsymbol{\sigma}_\eta = 2\eta \boldsymbol{D}_\eta - pI & \text{in } \Omega \ , \\ q_\phi = -M_\phi \mu & \text{in } \Omega \ , \\ \mathbf{F}_\phi = \mu \nabla \phi + \nabla \cdot (\lambda \delta_\gamma \mathcal{P}) & \text{in } \Omega \ , \\ J_\Gamma = -\kappa_\Gamma^{-1} \hat{L}(\phi) & \text{on } \partial\Omega_w \ , \\ u_{\tau_i} = \beta_s^{-1}(-(\mathbf{n} \cdot (\boldsymbol{\sigma}_\eta + \lambda \delta_\gamma \mathcal{P}) \cdot \boldsymbol{\tau}_i) + \hat{L}(\phi) \partial_{\tau_i} \phi) \ , \ i = 1, 2, & \text{on } \partial\Omega_w \ . \end{cases} \tag{2.14}$$

Here constant M_ϕ is called the mobility (a phenomenological parameter), κ_γ is the boundary mobility (a phenomenological parameter), and β_s is the wall friction coefficient.

To this end, the proposed phase-field model is composed of the following equations:

$$\begin{cases} \dfrac{\partial \phi}{\partial t} + \nabla \cdot (\mathbf{u}\phi) = -M_\phi \mu \ , \\ \mu = \dfrac{\hat{\kappa}_B}{\gamma^3} g(\phi) + M_v \dfrac{V(\phi) - V(\phi_0)}{V(\phi_0)} + \dfrac{M_s}{\gamma} \dfrac{S(\phi) - S(\phi_0)}{S(\phi_0)} f(\phi) \ , \\ g(\phi) = -\gamma^2 \Delta f + (3\phi^2 - 1) f(\phi), \\ f(\phi) = -\gamma^2 \Delta \phi + (\phi^2 - 1)\phi \ , \\ \rho \left(\dfrac{\partial \mathbf{u}}{\partial t} + (\mathbf{u} \cdot \nabla)\mathbf{u} \right) + \nabla p = \nabla \cdot (2\eta \boldsymbol{D}_\eta) + \mu \nabla \phi + \nabla \cdot (\lambda \delta_\gamma \mathcal{P}) \ , \\ \nabla \cdot \mathbf{u} = 0 \ , \\ \delta_\gamma (\mathcal{P} : \nabla \mathbf{u}) + \xi \gamma^2 \nabla \cdot (\phi^2 \nabla \lambda) = 0 \end{cases} \tag{2.15}$$

with the boundary conditions

$$\begin{cases} \mathbf{u} \cdot \mathbf{n} = 0 \ , \\ -\beta_s u_{\tau_i} = (\mathbf{n} \cdot (\boldsymbol{\sigma}_\eta + \lambda \delta_\gamma \mathcal{P}) \cdot \boldsymbol{\tau}_i) - \hat{L}(\phi) \partial_{\tau_i} \phi \ , \ i = 1, 2, \\ f = 0 \ , \\ \kappa_\Gamma \left(\dfrac{\partial \phi}{\partial t} + \mathbf{u} \cdot \nabla_\Gamma \phi \right) = -\hat{L}(\phi) \ , \\ \hat{L}(\phi) = \dfrac{\hat{\kappa}_B}{\gamma} \partial_n f + M_s \dfrac{S(\phi) - S(\phi_0)}{S(\phi_0)} \gamma \partial_n \phi + \dfrac{\partial f_w}{\partial \phi} \ , \\ \partial_n \lambda = 0 \ . \end{cases} \tag{2.16}$$

3. Dimensionless model governing equations and energy dissipation law. If the viscosity, length, velocity, time, bulk, and boundary chemical potentials in (2.15)–(2.16) are scaled by their corresponding characteristic values η_0, L, U, $\frac{L}{U}$ $\frac{\eta_0 U}{L}$ and $\eta_0 U$, respectively, and if we let $\varepsilon = \frac{\gamma}{L}$ be the nondimensionalized thickness of the interface (2.15)–(2.16) can be rewritten as

$$\begin{cases} Re \left(\dfrac{\partial \mathbf{u}}{\partial t} + (\mathbf{u} \cdot \nabla)\mathbf{u} \right) + \nabla P = \nabla \cdot (2\eta \boldsymbol{D}) + \mu \nabla \phi + \nabla \cdot (\lambda \delta_\epsilon \mathcal{P}) & \text{in } \Omega \ , \\ \nabla \cdot \mathbf{u} = 0 & \text{in } \Omega \ , \\ \dfrac{\partial \phi}{\partial t} + \mathbf{u} \cdot \nabla \phi = -\mathcal{M} \mu & \text{in } \Omega \ , \\ \mu = \kappa_B g(\phi) + \mathcal{M}_v \dfrac{(V(\phi) - V(\phi_0))}{V(\phi_0)} + \mathcal{M}_s \dfrac{(S(\phi) - S(\phi_0))}{S(\phi_0)} f(\phi) & \text{in } \Omega \ , \\ f(\phi) = -\epsilon \Delta \phi + \dfrac{(\phi^2 - 1)}{\epsilon} \phi, \ g(\phi) = -\Delta f + \dfrac{1}{\epsilon^2}(3\phi^2 - 1) f(\phi) & \text{in } \Omega \ , \\ \delta_\epsilon (\mathcal{P} : \nabla \mathbf{u}) + \xi \varepsilon^2 \nabla \cdot (\phi^2 \nabla \lambda) = 0 & \text{in } \Omega \end{cases} \tag{3.1}$$

with the boundary conditions

$$
\begin{cases}
\kappa\dot{\phi} + L(\phi) = 0 & \text{on } \partial\Omega_w \ , \\
L(\phi) = \kappa_B \partial_n f + \epsilon \mathcal{M}_s \dfrac{S(\phi) - S(\phi_0)}{S(\phi_0)} \partial_n \phi + \alpha_w \dfrac{df_w}{d\phi} & \text{on } \partial\Omega_w \ , \\
-l_s^{-1} u_{\tau_i} = \boldsymbol{\tau_i} \cdot (2\eta \mathbf{D}_\eta + \lambda \delta_\epsilon \mathcal{P}) \cdot \boldsymbol{n} - L(\phi) \partial_{\tau_i} \phi \ , \ i = 1, 2, & \text{on } \partial\Omega_w \ , \\
f = 0 & \text{on } \partial\Omega_w \ , \\
\partial_n \lambda = 0 & \text{on } \partial\Omega_w \ ,
\end{cases} \tag{3.2}
$$

where $V(\phi) = \int_\Omega \phi d\boldsymbol{x}$, $S(\phi) = \int_\Omega \frac{\epsilon}{2}|\nabla\phi|^2 + \frac{1}{4\epsilon}(\phi^2-1)^2 d\boldsymbol{x}$, and $\delta_\epsilon = \frac{1}{2}\epsilon^2|\nabla\phi|^2$. The dimensionless constants in (3.1)–(3.2) are given by $\epsilon = \frac{\gamma}{L}$, $Re = \frac{\rho_0 U L}{\eta_0}$, $\mathcal{M} = M_\phi \eta_0$, $\kappa_B = \frac{\hat{\kappa}_B}{L^2 \eta_0 U}$, $k = \frac{\hat{\kappa}_B}{\eta_0 L}$, $l_s = \frac{\eta_0}{\beta_s L}$, $\alpha_w = \frac{\sigma}{\eta_0 U}$, $\mathcal{M}_s = \frac{M_s}{\eta_0 U}$, and $\mathcal{M}_v = \frac{M_v L}{\eta_0 U}$.

If we define the Sobolev spaces as [22, 53]

$$
\boldsymbol{W}^{1,3} = (W^{1,3})^2 \ , \tag{3.3}
$$

$$
\boldsymbol{W}^{1,3}(\Omega) = \left\{ \mathbf{u} = (u_x, u_y)^T \in \boldsymbol{W}^{1,3} | \mathbf{u} \cdot \boldsymbol{n} = 0, \text{ on } \partial\Omega_w \right\} \ , \tag{3.4}
$$

$$
\boldsymbol{W}_b = W^{1,3}(\Omega) \times W^{1,3}(\Omega) \times W^{1,3}(\Omega) \times W^{1,3/2}(\Omega) \times W^{1,3/2}(\Omega) \times \boldsymbol{W}^{1,3}(\Omega) \tag{3.5}
$$

and let $\|\cdot\| = (\int_\Omega |\cdot|^2 d\boldsymbol{x})^{\frac{1}{2}}$ and $\|\cdot\|_w = (\int_{\partial\Omega_w} |\cdot|^2 ds)^{\frac{1}{2}}$ denote the L^2 norm defined in the domain and on the domain boundary, respectively, then the system (3.1)–(3.2) satisfies the following energy law.

THEOREM 3.1. *If* $(\phi,\ f,\ \mu,\ \lambda,\ P,\ \mathbf{u}) \in \boldsymbol{W}_b$ *are smooth solutions of the above system* (3.1)–(3.2)*, then the following energy law is satisfied:*

$$
\begin{aligned}
\frac{d}{dt}\mathcal{E}_{total} &= \frac{d}{dt}(\mathcal{E}_{kin} + \mathcal{E}_{cell} + \mathcal{E}_w) \\
&= \frac{1}{Re}\left(-2\|\eta^{1/2}\mathbf{D}_\eta\|^2 - \mathcal{M}\|\mu\|^2 - \xi\|\epsilon\phi\nabla\lambda\|^2 - \kappa\|\dot{\phi}\|_w^2 - \|l_s^{-1/2}\mathbf{u}_\tau\|_w^2 \right) \ ,
\end{aligned} \tag{3.6}
$$

where $\mathcal{E}_{total} = \mathcal{E}_{kin} + \mathcal{E}_{cell} + \mathcal{E}_w$, $\mathcal{E}_{kin} = \frac{1}{2}\int_\Omega |\mathbf{u}|^2 d\boldsymbol{x}$, $\mathcal{E}_{cell} = \frac{\kappa_B}{2Re\epsilon}\int_\Omega |f|^2 d\boldsymbol{x} + \mathcal{M}_v \frac{(V(\phi)-V(\phi_0))^2}{2ReV(\phi_0)} + \mathcal{M}_s \frac{(S(\phi)-S(\phi_0))^2}{2ReS(\phi_0)}$*, and* $\mathcal{E}_w = \frac{\alpha_w}{Re}\int_{\partial\Omega_w} f_w ds$*.*

Proof. Multiplying the first equation in (3.1) with $\mathbf{u}$ and integration by parts yield

$$
\begin{aligned}
\frac{d}{dt}\mathcal{E}_{kin} &= \frac{1}{Re}\left\{ -\int_\Omega 2\eta|\boldsymbol{D}_\eta|^2 d\boldsymbol{x} + \int_{\partial\Omega_w} (\boldsymbol{\sigma}_\eta \cdot \mathbf{n}) \cdot \mathbf{u}_\tau ds + \int_\Omega \mu\nabla\phi \cdot \mathbf{u} d\boldsymbol{x} \right. \\
&\qquad \left. - \int_\Omega \lambda\delta_\epsilon \mathcal{P} : \nabla\mathbf{u} d\boldsymbol{x} + \int_{\partial\Omega_w} (\lambda\delta_\epsilon\mathcal{P}\cdot\mathbf{n}) \cdot \mathbf{u}_\tau ds \right\} \\
&= \frac{1}{Re}\left\{ -\int_\Omega 2\eta|\boldsymbol{D}_\eta|^2 d\boldsymbol{x} - \int_\Omega \lambda\delta_\epsilon\mathcal{P} : \nabla\mathbf{u} d\boldsymbol{x} - l_s^{-1}\int_{\partial\Omega_w} |\mathbf{u}_\tau|^2 ds \right. \\
&\qquad \left. + \int_{\partial\Omega_w} L(\phi)\partial_\tau\phi \cdot \mathbf{u}_\tau ds + \int_\Omega \mu\nabla\phi\cdot\mathbf{u} d\boldsymbol{x} \right\},
\end{aligned} \tag{3.7}
$$

where the slip boundary condition in (3.2) is applied.

Taking the inner product of the third equation in (3.1) with $\frac{\mu}{Re}$ results in

$$
\frac{1}{Re}\int_\Omega \frac{\partial\phi}{\partial t}\mu d\boldsymbol{x} + \frac{1}{Re}\int_\Omega \mathbf{u}\cdot\nabla\phi\mu d\boldsymbol{x} = -\frac{1}{Re}\mathcal{M}\int_\Omega |\mu|^2 d\boldsymbol{x} \ . \tag{3.8}
$$

Multiplying the fourth equation in (3.1) with $\frac{1}{Re}\frac{\partial \phi}{\partial t}$ and integration by parts give rise to

(3.9)
$$\begin{aligned}\frac{1}{Re}\int_\Omega \mu\frac{\partial \phi}{\partial t}d\boldsymbol{x} &= \frac{1}{Re}\left\{\kappa_B\int_\Omega g\frac{\partial \phi}{\partial t}d\boldsymbol{x}+\frac{d}{dt}\left(\mathcal{M}_v\frac{(V(\phi)-V(\phi_0))^2}{2V(\phi_0)}\right)\right.\\ &\qquad\left.+\mathcal{M}_s\frac{S(\phi)-S(\phi_0)}{S(\phi_0)}\int_\Omega f\frac{\partial \phi}{\partial t}d\boldsymbol{x}\right\}\\ &= \frac{\kappa_B}{Re}\int_\Omega f\frac{\partial}{\partial t}\left(-\Delta\phi+\frac{1}{\epsilon^2}(\phi^3-\phi)\right)d\boldsymbol{x}-\frac{\kappa_B}{Re}\int_{\partial\Omega_w}\partial_n f\frac{\partial \phi}{\partial t}ds\\ &\quad+\frac{d}{dt}\left(\mathcal{M}_v\frac{(V(\phi)-V(\phi_0))^2}{ReV(\phi_0)}\right)+\mathcal{M}_s\frac{d}{dt}\left(\frac{(S(\phi)-S(\phi_0))^2}{2ReS(\phi_0)}\right)\\ &\quad-\mathcal{M}_s\left(\frac{S(\phi)-S(\phi_0)}{ReS(\phi_0)}\right)\int_{\partial\Omega_w}\epsilon\partial_n\phi\frac{\partial \phi}{\partial t}ds\\ &= \frac{d}{dt}\left(\kappa_B\int_\Omega\frac{|f|^2}{2Re\epsilon}d\boldsymbol{x}\right)+\frac{d}{dt}\left(\mathcal{M}_v\frac{(V(\phi)-V(\phi_0))^2}{2ReV(\phi_0)}\right)\\ &\quad+\mathcal{M}_s\frac{d}{dt}\left(\frac{(S(\phi)-S(\phi_0))^2}{2ReS(\phi_0)}\right)-\int_{\partial\Omega_w}\frac{L(\phi)}{Re}\frac{\partial \phi}{\partial t}ds+\frac{\alpha_w}{Re}\frac{d}{dt}\int_{\partial\Omega_w}f_w ds\\ &= \frac{d}{dt}(\mathcal{E}_{cell}+\mathcal{E}_w)-\int_{\partial\Omega_w}\frac{L(\phi)}{Re}\frac{\partial \phi}{\partial t}ds\ ,\end{aligned}$$

where the definitions of $f(\phi)$, $g(\phi)$ and the boundary conditions of ϕ and f are utilized.

Multiplying the last equations with $\frac{\lambda}{Re}$ and integration by parts lead to

$$\frac{1}{Re}\int_\Omega(\lambda\delta_\epsilon\mathcal{P}):\nabla\mathbf{u}d\boldsymbol{x}-\frac{1}{Re}\int_\Omega\xi\varepsilon^2\phi^2(\nabla\lambda)^2=0\ . \tag{3.10}$$

Finally, the energy dissipation law (3.6) is obtained by combining (3.7), (3.8), (3.9), and (3.10). ∎

4. Numerical scheme and discrete energy law.

4.1. Time-discrete primitive method. The numerical scheme for solving (3.1)–(3.2) uses the midpoint method for temporal discretization. Let Δt denote the time step size, and let $()^{n+1}$ and $()^n$ denote the value of the variables at times $(n+1)\Delta t$ and $n\Delta t$, respectively. The semidiscrete in time equations are as follows: in Ω,

(4.1)
$$\begin{cases}\dfrac{\mathbf{u}^{n+1}-\mathbf{u}^n}{\Delta t}+\left(\mathbf{u}^{n+\frac12}\cdot\nabla\right)\mathbf{u}^{n+\frac12}+\dfrac{1}{Re}\nabla P^{n+\frac12}=\dfrac{1}{Re}\nabla\cdot\left(\eta^n\left(\nabla\mathbf{u}^{n+\frac12}+(\nabla\mathbf{u}^{n+\frac12})^T\right)\right)\\ \qquad+\dfrac{1}{Re}\mu^{n+\frac12}\nabla\phi^{n+\frac12}+\dfrac{1}{Re}\nabla\cdot\left(\lambda^{n+\frac12}\mathcal{P}^n\delta_\epsilon\right)\ ,\\ \nabla\cdot\mathbf{u}^{n+\frac12}=0\ ,\\ \dfrac{\phi^{n+1}-\phi^n}{\Delta t}+\left(\mathbf{u}^{n+\frac12}\cdot\nabla\right)\phi^{n+\frac12}=-\mathcal{M}\mu^{n+\frac12}\ ,\\ \mu^{n+\frac12}=\kappa_B g\left(\phi^{n+1},\phi^n\right)+\mathcal{M}_v\dfrac{\left(V\left(\phi^{n+\frac12}\right)-V(\phi_0)\right)}{V(\phi_0)}\\ \qquad+\mathcal{M}_s\dfrac{\left(S\left(\phi^{n+\frac12}\right)-S(\phi_0)\right)}{S(G_0)}f\left(\phi^{n+1},\phi^n\right)\ ,\\ f^{n+\frac12}=-\epsilon\Delta\phi^{n+\frac12}+\dfrac{1}{\epsilon}\left(\left(\phi^{n+\frac12}\right)^2-1\right)\phi^{n+\frac12}\ ,\\ \xi\epsilon^2\nabla\cdot\left((\phi^n)^2\nabla\lambda^{n+\frac12}\right)+\delta_\epsilon\mathcal{P}^n:\nabla\mathbf{u}^{n+\frac12}=0\ .\end{cases}$$

The numerical boundary conditions can be written as

(4.2)
$$\begin{cases} \kappa\dot{\phi}^{n+\frac{1}{2}} = -L^{n+\frac{1}{2}} & \text{on } \partial\Omega_w, \\ L^{n+\frac{1}{2}} = \kappa_B\partial_n f^{n+\frac{1}{2}} + \mathcal{M}_s\epsilon\dfrac{S\left(\phi^{n+\frac{1}{2}}\right)-S_0}{S_0}\partial_n\phi^{n+\frac{1}{2}} + \alpha_w\dfrac{f_w^{n+1}-f_w^n}{\phi^{n+1}-\phi^n} & \text{on } \partial\Omega_w, \\ -l_s^{-1}u_{\tau_i}^{n+\frac{1}{2}} = \boldsymbol{\tau_i}\cdot\left(\eta^n\left(\nabla\mathbf{u}^{n+\frac{1}{2}}+\left(\nabla\mathbf{u}^{n+\frac{1}{2}}\right)^T\right)+\lambda^{n+\frac{1}{2}}\delta_\epsilon\mathcal{P}^n\right)\cdot\boldsymbol{n} \\ \qquad\qquad -L^{n+\frac{1}{2}}\partial_{\tau_i}\phi^{n+\frac{1}{2}}\ , \quad i=1,2, & \text{on } \partial\Omega_w, \\ f^{n+\frac{1}{2}} = 0 & \text{on } \partial\Omega_w, \\ \partial_n\lambda^{n+\frac{1}{2}} = 0 & \text{on } \partial\Omega_w, \end{cases}$$

where

$$f\left(\phi^{n+1},\phi^n\right) = -\epsilon\Delta\phi^{n+\frac{1}{2}} + \frac{1}{4\epsilon}\left(\left(\phi^{n+1}\right)^2+(\phi^n)^2-2\right)\left(\phi^{n+1}+\phi^n\right), \tag{4.3}$$

$$g\left(\phi^{n+1},\phi^n\right) = \left(-\Delta f^{n+\frac{1}{2}} + \frac{1}{\epsilon^2}\left(\left(\phi^{n+1}\right)^2+(\phi^n)^2+\phi^{n+1}\phi^n-1\right)f^{n+\frac{1}{2}}\right), \tag{4.4}$$

$(\cdot)^{n+\frac{1}{2}} = \frac{(\cdot)^n+(\cdot)^{n+1}}{2}$, and $\mathcal{P}^n = I - \mathbf{n}_m^n\otimes\mathbf{n}_m^n$ with $\mathbf{n}_m^n = \frac{\nabla\phi^n}{|\nabla\phi^n|}$.

The above scheme obeys the following theorem of energy stability.

THEOREM 4.1. *If $(\phi^n,\mathbf{u}^n,P^n)$ are smooth solutions of the above system (4.1)–(4.2), then the following energy law is satisfied:*

$$\begin{aligned} \mathcal{E}_{total}^{n+1}-\mathcal{E}_{total}^n &= \left(\mathcal{E}_{kin}^{n+1}+\mathcal{E}_{cell}^{n+1}+\mathcal{E}_w^{n+1}\right)-\left(\mathcal{E}_{kin}^n+\mathcal{E}_{cell}^n+\mathcal{E}_w^n\right) \\ &= \frac{\triangle t}{Re}\left(-2\|(\eta^n)^{1/2}\mathbf{D}_\eta^{n+\frac{1}{2}}\|^2-\mathcal{M}\|\mu^{n+\frac{1}{2}}\|^2-\xi\|\ \epsilon\phi^n\nabla\lambda^{n+\frac{1}{2}}\|^2\right. \\ &\quad \left.-\frac{1}{\kappa}\|L(\phi^{n+\frac{1}{2}})\|_w^2-\|l_s^{-1/2}\mathbf{u}_\tau^{n+\frac{1}{2}}\|_w^2\right)\ , \end{aligned} \tag{4.5}$$

where $\mathcal{E}_{total}^n = \mathcal{E}_{kin}^n+\mathcal{E}_{cell}^n+\mathcal{E}_w^n$ with $\mathcal{E}_{kin}^n = \frac{1}{2}\|\mathbf{u}^n\|^2$, $\mathcal{E}_{cell}^n = \frac{\kappa_B\|f^n\|^2}{2Re\epsilon}+\mathcal{M}_v\frac{(V(\phi^n)-V(\phi_0))^2}{2ReV(\phi_0)}$ $+\mathcal{M}_s\frac{(S(\phi^n)-S(\phi_0))^2}{2ReS(\phi_0)}$, and $\mathcal{E}_w^n = \frac{\alpha_w}{Re}\int_{\partial\Omega_w}f_w^n ds$.

The following two lemmas are needed for proving Theorem 4.1. Proofs of these two lemmas can be found in the appendix.

LEMMA 4.2. *Let*

$$f\left(\phi^{n+1},\phi^n\right) = -\epsilon\Delta\phi^{n+\frac{1}{2}} + \frac{1}{4\epsilon}\left(\left(\phi^{n+1}\right)^2+(\phi^n)^2-2\right)\left(\phi^{n+1}+\phi^n\right). \tag{4.6}$$

Then $f(\phi^{n+1},\phi^n)$ satisfies

$$\int_\Omega f\left(\phi^{n+1},\phi^n\right)\left(\phi^{n+1}-\phi^n\right)d\boldsymbol{x} = S^{n+1}-S^n-\int_{\partial\Omega_w}\epsilon\partial_n\phi^{n+\frac{1}{2}}\left(\phi^{n+1}-\phi^n\right)ds, \tag{4.7}$$

where $S^{n+1} = \int_\Omega G(\phi^{n+1})d\boldsymbol{x}, S^n = \int_\Omega G(\phi^n)d\boldsymbol{x}$.

LEMMA 4.3. *Let $g(\phi^{n+1},\phi^n) = -\Delta f^{n+\frac{1}{2}}+\frac{1}{\epsilon^2}((\phi^{n+1})^2+(\phi^n)^2+\phi^{n+1}\phi^n-1)f^{n+\frac{1}{2}}$. Then $g(\phi^{n+1},\phi^n)$ satisfies*

$$\int_\Omega g\left(\phi^{n+1},\phi^n\right)\left(\phi^{n+1}-\phi^n\right)d\boldsymbol{x}$$

$$= \int_\Omega \frac{1}{2\epsilon}((f^{n+1})^2-(f^n)^2)d\boldsymbol{x} - \int_{\partial\Omega_w}\partial_n f^{n+\frac{1}{2}}(\phi^{n+1}-\phi^n)ds\ , \tag{4.8}$$

where $f^{n+1}=-\epsilon\Delta\phi^{n+1}+\frac{1}{\epsilon}((\phi^{n+1})^2-1)\phi^{n+1}$, $f^n=-\epsilon\Delta\phi^n+\frac{1}{\epsilon}((\phi^n)^2-1)\phi^n$.

Proof of Theorem 4.1. Multiplying the first equation in system (4.1) by $\Delta t\mathbf{u}^{n+\frac{1}{2}}$ gives

(4.9)

$$\begin{aligned}
&\int_\Omega \frac{1}{2}((\mathbf{u}^{n+1})^2-(\mathbf{u}^n)^2)d\boldsymbol{x} + \int_\Omega \Delta t\mathbf{u}^{n+\frac{1}{2}}\cdot\left(\left(\mathbf{u}^{n+\frac{1}{2}}\nabla\right)\cdot\mathbf{u}^{n+\frac{1}{2}}\right)d\boldsymbol{x}\\
&\quad -\frac{\Delta t}{Re}\int_\Omega P^{n+\frac{1}{2}}\nabla\cdot\mathbf{u}^{n+\frac{1}{2}}d\boldsymbol{x}\\
&= -\frac{\Delta t}{Re}\int_\Omega \nabla\mathbf{u}^{n+\frac{1}{2}}:\eta^n\left(\nabla\mathbf{u}^{n+\frac{1}{2}}+\left(\nabla\mathbf{u}^{n+\frac{1}{2}}\right)^T\right)d\boldsymbol{x} + \frac{\Delta t}{Re}\int_\Omega \mathbf{u}^{n+\frac{1}{2}}\cdot\nabla\phi^{n+1}\mu^{n+1}d\boldsymbol{x}\\
&\quad -\frac{\Delta t}{Re}\int_\Omega \lambda\delta_\epsilon\mathcal{P}^n:\nabla\mathbf{u}^{n+\frac{1}{2}}d\boldsymbol{x} + \frac{\Delta t}{Re}\int_{\partial\Omega_w}\lambda^{n+\frac{1}{2}}(\delta_\epsilon\mathcal{P}^n\cdot\mathbf{n})\cdot\mathbf{u}_\tau^{n+\frac{1}{2}}ds\\
&\quad +\frac{\Delta t}{Re}\int_{\partial\Omega_w}\mathbf{u}^{n+\frac{1}{2}}\cdot\eta^n\left(\left(\nabla\mathbf{u}^{n+\frac{1}{2}}+(\nabla\mathbf{u}^{n+\frac{1}{2}})^T\right)\cdot\boldsymbol{n}\right)ds.
\end{aligned}$$

Multiplying the fourth equation in system (4.1) by $\frac{\phi^{n+1}-\phi^n}{Re}$ and integration by parts lead to

(4.10)

$$\begin{aligned}
&\frac{1}{Re}\int_\Omega \mu^{n+1/2}\left(\phi^{n+1}-\phi^n\right)d\boldsymbol{x} = \frac{\kappa_B}{Re}\int_\Omega\frac{1}{2\epsilon}((f^{n+1})^2-(f^n)^2)d\boldsymbol{x}\\
&\quad +\frac{\mathcal{M}_v}{Re}\frac{(V\left(\phi^{n+1}\right)-V_0)^2-(V(\phi^n)-V_0)^2}{2V_0}+\frac{\mathcal{M}_s}{Re}\frac{(S\left(\phi^{n+1}\right)-S_0)^2-(S(\phi^n)-S_0)^2}{2S_0}\\
&\quad -\frac{\kappa_B}{Re}\int_{\partial\Omega_w}\partial_n f^{n+\frac{1}{2}}\left(\phi^{n+1}-\phi^n\right)ds - \frac{\mathcal{M}_s}{Re}\int_{\partial\Omega_w}\frac{S\left(\phi^{n+\frac{1}{2}}\right)-S_0}{S_0}\epsilon\partial_n\phi^{n+\frac{1}{2}}\left(\phi^{n+1}-\phi^n\right)ds.
\end{aligned}$$

Multiplying the third equation in system (4.1) by $\frac{\mu^{n+1}\Delta t}{Re}$ and integration by parts yield

$$\begin{aligned}
&\frac{1}{Re}\int_\Omega \mu^{n+1}\left(\phi^{n+1}-\phi^n\right)d\boldsymbol{x} + \frac{\Delta t}{Re}\int_\Omega \mu^{n+1}(\mathbf{u}^{n+1/2}\cdot\nabla)\phi^{n+1}d\boldsymbol{x}\\
&= -\frac{\mathcal{M}\Delta t}{Re}\int_\Omega(\mu^{n+1})^2d\boldsymbol{x}.
\end{aligned}\tag{4.11}$$

Multiplying the last equation in system (4.1) by $\frac{\lambda^{n+\frac{1}{2}}\Delta t}{Re}$ and integration by parts give

$$-\frac{\Delta t}{Re}\int_\Omega \xi\epsilon^2(\phi^n)^2\left|\nabla\lambda^{n+\frac{1}{2}}\right|^2d\boldsymbol{x} + \frac{\Delta t}{Re}\int_\Omega(\lambda^{n+\frac{1}{2}}\delta_\epsilon\mathcal{P}^n):\nabla\mathbf{u}^{n+\frac{1}{2}}d\boldsymbol{x}=0. \tag{4.12}$$

The discretized energy dissipation law (4.5) is obtained by combining (4.9)–(4.12) and organizing the terms according to the boundary conditions $L(\phi)$ as shown in (4.2). ∎

Remark 4.4. The system (4.1) is second-order accurate in time except for the last equation. It can be changed to be second-order accurate as well by using $\phi^{n+1/2}$ and $\mathcal{P}^{n+1/2}$. However, this change makes the Newton iteration discussed in the next section very complicated. For simplicity of computer implementation, a first-order accurate treatment for the last equation is adopted here.

4.2. Fully discrete C^0 finite element scheme. The spatial discretization using C^0 finite element is straightforward. Let Ω be the domain of interest with a Lipschitz-continuous boundary $\partial\Omega$. Let ${\mathbf{W}_b}^h \subset \mathbf{W}_b$ be a finite element space with respect to the triangulation of the domain Ω. The fully discrete scheme of the system is to find $({\phi_h}^{n+1}, {\mu_h}^{n+1}, {f_h}^{n+1}, {\lambda_h}^{n+1}, {p_h}^{n+1}, {\mathbf{u}_h}^{n+1}) \in {\mathbf{W}_b}^h$, such that for any $(\psi_h, \chi_h, \zeta_h, \Theta_h, q_h, \mathbf{v}_h) \in \mathbf{W}_b^h$,

(4.13)

$$
\begin{cases}
\displaystyle\int_\Omega \left(\frac{\mathbf{u}_h^{n+1} - \mathbf{u}_h^n}{\Delta t} + \left(\mathbf{u}_h^{n+\frac{1}{2}} \cdot \nabla\right) \mathbf{u}_h^{n+\frac{1}{2}} + \frac{1}{Re} \nabla P_h^{n+\frac{1}{2}} \right) \cdot \mathbf{v}_h d\boldsymbol{x} \\
\quad = -\displaystyle\int_\Omega \frac{1}{Re} \left(\eta_h^n \left(\nabla \mathbf{u}_h^{n+\frac{1}{2}} + \left(\nabla \mathbf{u}_h^{n+\frac{1}{2}}\right)^T \right) \right) : \nabla \mathbf{v}_h d\boldsymbol{x} \\
\qquad + \displaystyle\int_\Omega \frac{1}{Re} \mu_h^{n+\frac{1}{2}} \nabla \phi_h^{n+\frac{1}{2}} \cdot \mathbf{v}_h d\boldsymbol{x} - \int_\Omega \frac{1}{Re} \lambda_h^{n+\frac{1}{2}} \mathcal{P}_h^n \delta_\epsilon : \mathbf{v}_h d\boldsymbol{x} \\
\qquad + \displaystyle\int_{\partial\Omega_w} \frac{1}{Re} \mathbf{n} \cdot \left(\eta_h^n \left(\nabla \mathbf{u}_h^{n+\frac{1}{2}} + \left(\nabla \mathbf{u}_h^{n+\frac{1}{2}}\right)^T \right) + \lambda_h^{n+\frac{1}{2}} \mathcal{P}_h^n \delta_\epsilon \right) \cdot \mathbf{v}_h d\boldsymbol{x} \ , \\
\displaystyle\int_\Omega \left(\nabla \cdot \mathbf{u}_h^{n+\frac{1}{2}} \right) q_h d\boldsymbol{x} = 0 \ , \\
\displaystyle\int_\Omega \left(\frac{\phi_h^{n+1} - \phi_h^n}{\Delta t} + \left(\mathbf{u}_h^{n+\frac{1}{2}} \cdot \nabla\right) \phi_h^{n+\frac{1}{2}} \right) \psi_h d\boldsymbol{x} = -\int_\Omega \mathcal{M} \mu_h^{n+\frac{1}{2}} \psi_h d\boldsymbol{x} \ , \\
\displaystyle\int_\Omega \mu_h^{n+\frac{1}{2}} \chi_h d\boldsymbol{x} = \int_\Omega \left(\kappa_B \frac{1}{\epsilon^2} \left(\left(\phi_h^{n+1}\right)^2 + \left(\phi_h^n\right)^2 + \phi_h^{n+1} \phi_h^n - 1 \right) f_h^{n+\frac{1}{2}} \right. \\
\qquad + \mathcal{M}_v \dfrac{\left(V\left(\phi_h^{n+\frac{1}{2}}\right) - V\left(\phi_0\right) \right)}{V\left(\phi_0\right)} \\
\qquad \left. + \mathcal{M}_s \dfrac{\left(S\left(\phi_h^{n+\frac{1}{2}}\right) - S(\phi_0) \right)}{S(G_0)} \left(\frac{1}{4\epsilon} \left(\left(\phi_h^{n+1}\right)^2 + \left(\phi_h^n\right)^2 - 2 \right) \left(\phi_h^{n+1} + \phi_h^n \right) \right) \right) \chi_h d\boldsymbol{x} \\
\qquad + \displaystyle\int_\Omega \left(\kappa_B \nabla f_h^{n+\frac{1}{2}} + \mathcal{M}_s \epsilon \frac{\left(S\left(\phi_h^{n+\frac{1}{2}}\right) - S\left(\phi_0\right) \right)}{S(G_0)} \nabla \phi_h^{n+\frac{1}{2}} \right) \cdot \nabla \chi_h d\boldsymbol{x} \\
\qquad - \displaystyle\int_{\partial\Omega_w} \left(\kappa_B \partial_{\mathbf{n}} f_h^{n+\frac{1}{2}} + \mathcal{M}_s \epsilon \frac{\left(S\left(\phi_h^{n+\frac{1}{2}}\right) - S\left(\phi_0\right) \right)}{S(G_0)} \partial_{\mathbf{n}} \phi_h^{n+\frac{1}{2}} \right) \chi_h d\boldsymbol{x} \ , \\
\displaystyle\int_\Omega f_h^{n+\frac{1}{2}} \zeta_h = \int_\Omega \epsilon \nabla \phi_h^{n+\frac{1}{2}} \cdot \nabla \zeta_h + \int_\Omega \frac{1}{\epsilon} \left(\left(\phi_h^{n+\frac{1}{2}}\right)^2 - 1 \right) \phi_h^{n+\frac{1}{2}} \zeta_h d\boldsymbol{x} \\
\qquad - \displaystyle\int_{\partial\Omega_w} \varepsilon \partial_{\mathbf{n}} \phi_h^{n+\frac{1}{2}} \zeta_h d\boldsymbol{x} \ , \\
\displaystyle\int_\Omega \xi \epsilon^2 \left(\left(\phi_h^n\right)^2 \nabla \lambda_h^{n+\frac{1}{2}} \right) \cdot \nabla \Theta_h dx = \int_\Omega \delta_\epsilon \mathcal{P}_h^n : \nabla \mathbf{u}_h^{n+\frac{1}{2}} \Theta_h d\boldsymbol{x} \\
\qquad + \displaystyle\int_{\partial\Omega_w} \xi \epsilon^2 \left(\left(\phi_h^n\right)^2 \partial_{\mathbf{n}} \lambda_h^{n+\frac{1}{2}} \right) \Theta_h d\boldsymbol{x} \ .
\end{cases}
$$

THEOREM 4.5. *If* $({\phi_h}^{n+1}, {\mu_h}^{n+1}, {f_h}^{n+1}, {\lambda_h}^{n+1}, {p_h}^{n+1}, {\mathbf{u}_h}^{n+1}) \in {\mathbf{W}_b}^h$ *are solutions of the above system, then the following energy law is satisfied:*

$$
\begin{aligned}
\mathcal{E}_{total,h}^{n+1} - \mathcal{E}_{total,h}^n = \frac{\triangle t}{Re} \Big(& -2 \|(\eta_h^n)^{1/2} \mathbf{D}_\eta^{n+\frac{1}{2}}\|^2 - \mathcal{M} \|\mu_h^{n+\frac{1}{2}}\|^2 - \xi \| \ \epsilon \phi_h^n \nabla \lambda_h^{n+\frac{1}{2}} \|^2 \\
& - \frac{1}{\kappa} \|L(\phi_h^{n+\frac{1}{2}})\|_w^2 - \|l_s^{-1/2} \mathbf{u}_{\tau,h}^{n+\frac{1}{2}}\|_w^2 \Big) .
\end{aligned} \tag{4.14}
$$

It is easy to prove this theorem by letting $\mathbf{v}_h = \Delta t \mathbf{u}_h^{n+1}$, $q_h = \frac{\Delta t p_h^{n+1}}{Re}$, $\psi_h = \frac{c_h^{n+1} - c_h^n}{Re}$, $\chi_h = \frac{\Delta t \mu_h^{n}+1}{Re}$, $\Theta_h = \frac{\Delta t \lambda_h^{n+1}}{Re}$ and following the process of proving Theorem 4.1. Details of the proof are presented in the appendix.

4.3. Linearization and unique solvability. Note that the energy stable scheme (4.13) is a coupled nonlinear system. Newton's method [22] is used to solve the scheme equations. First, the scheme (4.13) can be written into the form

$$\mathcal{F}_h^{n+1} = \mathcal{C}$$

by relocating all of the constant terms to the right-hand side and the terms containing unknown variables to the left-hand side.

For the sake of simplification, we let $\mathbb{U}_h^{n+1,k} = ({\phi_h}^{n+1,k}, {\mu_h}^{n+1,k}, {f_h}^{n+1,k}, {\lambda_h}^{n+1,k}, {\mathbf{u}_h}^{n+1,k}, {p_h}^{n+1,k})$ be the solution at time $(n+1)\Delta t$ in the kth iteration of Newton's method, and we let the variation between iterations be

$$(\delta\mathbb{U})_h^{n+1,k} = \big((\delta\phi_h)^{n+1,k+1}, (\delta\mu_h)^{n+1,k+1}, (\delta f_h)^{n+1,k+1}, (\delta\lambda_h)^{n+1,k+1}, (\delta\mathbf{u}_h)^{n+1,k+1}, (\delta p_h)^{n+1,k+1}\big) .$$

Here $(\delta\cdot)$ stands for the amount of change of the value, $(\delta\cdot)^{n+1,k} = (\cdot)^{n+1,k+1} - (\cdot)^{n+1,k}$. Newton's method can be formally written as

$$\mathcal{F}_h^{n+1}(\mathbb{U}_h^{n+1,k}) + \nabla_{\mathbb{U}_h^{n+1,k}} \mathcal{F}_h^{n+1}(\mathbb{U}_h^{n+1,k}) \cdot (\delta\mathbb{U})_h^{n+1,k} = \mathcal{C}(\mathbb{U}_h^n) .$$

The solution is updated by $\mathbb{U}_h^{n+1,k+1} = \mathbb{U}_h^{n+1,k} + \delta\mathbb{U}_h^{n+1,k}$, where $\mathbb{U}_h^{n+1,0} = \mathbb{U}_h^n$.

Then we have the following theorem for the solvability.

THEOREM 4.6. *If the time step Δt is small enough, then the equations of the scheme* (4.13) *are uniquely solvable.*

Proof. From the last three equations we find $\mu_h^{n+1} = \mu(\phi_h^{n+1})$, $f_h^{n+1} = f(\phi_h^{n+1})$, $\lambda_h^{n+1} = \lambda(\mathbf{u}_h^{n+1})$. With the first and the second equations, P_h^{n+1} can be expressed as $P_h^{n+1} = P(\mathbf{u}_h^{n+1}, \phi_h^{n+1})$. Then the first and the third equations can be solved separately. Applying Newton's method to the first three equations, we have their linearized form:

(4.15)
$$\mathcal{F}_h^{n+1}\left(\mathbf{u}_h^{n+1,k}, \phi_h^{n+1,k}\right) + \nabla_{\mathbf{u}_h^{n+1,k}, \phi_h^{n+1,k}} \mathcal{F}_h^{n+1}\left(\mathbf{u}_h^{n+1,k}, \phi_h^{n+1,k}\right) \cdot \left(\mathbf{u}_h^{n+1,k+1} - \mathbf{u}_h^{n+1,k}, \phi_h^{n+1,k+1} - \phi_h^{n+1,k}\right)^T = \mathcal{C}.$$

Note that $\mathbf{u}_h^{n+1,k+1} = (u_h^{n+1,k}, v_h^{n+1,k+1})$. Multiplying Δt to (4.15) yields

$$\begin{pmatrix} I - \Delta t A_{11} & \Delta t A_{12} & \Delta t A_{13} \\ \Delta t A_{21} & I - \Delta t A_{22} & \Delta t A_{23} \\ \Delta t A_{31} & \Delta t A_{32} & I - \Delta t A_{33} \end{pmatrix} \begin{pmatrix} u_h^{n+1,k+1} \\ v_h^{n+1,k+1} \\ \phi_h^{n+1,k+1} \end{pmatrix} = \mathcal{C}', \tag{4.16}$$

where

$A_{11} = \frac{1}{4}(u_h^{n+1,k}\partial_{x,h} + \partial_{x,h} u_h^{n+1,k} + u_h^n \partial_{x,h} + \partial_{x,h} u_h^n + \partial_{y,h} v_h^{n+1,k}) - \frac{1}{2Re}(2\partial_{x,h}(\eta_h^n \partial_{x,h}) + \partial_{y,h}(\eta_h^n \partial_{y,h})) + \frac{1}{2Re}\frac{\partial_h(\partial_{x,h} P_h^{n+1,k})}{\partial_h u_h^{n+1,k}} - \frac{1}{4Re}\frac{\partial_h(\partial_{x,h}(\lambda_h^{n+1,k}(\partial_{x,h}\phi_h^n)^2)) + \partial_{y,h}(\lambda_h^{n+1,k}\partial_{x,h}\phi_h^n \partial_{y,h}\phi_h^n)}{\partial u_h^{n+1,k}}$,

$A_{12} = \frac{1}{4} u_h^{n+1,k}\partial_{y,h} - \frac{1}{2Re}\eta_h^n \partial_{x,h}\partial_{y,h} + \frac{1}{2Re}\frac{\partial_h(\partial_{x,h} P_h^{n+1,k})}{\partial_h v_h^{n+1,k}}$

$$- \tfrac{1}{4Re}\tfrac{\partial_h(\partial_{x,h}(\lambda_h^{n+1,k}(\partial_{x,h}\phi_h^n)^2))+\partial_{y,h}(\lambda_h^{n+1,k}\partial_{x,h}\phi_h^n\partial_{y,h}\phi_h^n)}{\partial v_h^{n+1,k}} ,$$

$$A_{13} = -\tfrac{1}{4Re}(\mu_h^{n+1,k}\partial_{x,h} + \tfrac{\partial\mu_h^{n+1,k}}{\partial\phi_h^{n+1,k}}\partial_{x,h}\phi_h^{n+1,k} + \mu_h^n\partial_{x,h} + \tfrac{\partial\mu_h^{n+1,k}}{\partial\phi_h^{n+1,k}}\partial_{x,h}\phi_h^n) ,$$

$$A_{21} = \tfrac{1}{4}v_h^{n+1,k}\partial_{x,h} - \tfrac{1}{2Re}\eta_h^n\partial_{x,h}\partial_{y,h} + \tfrac{1}{2Re}\tfrac{\partial_h(\partial_{y,h}P_h^{n+1,k})}{\partial_h u_h^{n+1,k}}$$

$$- \tfrac{1}{4Re}\tfrac{\partial_h(\partial_{y,h}(\lambda_h^{n+1,k}(\partial_{y,h}\phi_h^n)^2))+\partial_{x,h}(\lambda_h^{n+1,k}\partial_{x,h}\phi_h^n\partial_{y,h}\phi_h^n)}{\partial u_h^{n+1,k}} ,$$

$$A_{22} = \tfrac{1}{4}(v_h^{n+1,k}\partial_{y,h} + \partial_{y,h}v_h^{n+1,k} + v_h^n\partial_{y,h} + \partial_{y,h}v_h^n + \partial_{x,h}u_h^{n+1,k}) - \tfrac{1}{2Re}(\partial_{x,h}(\eta_h^n\partial_{x,h}) +$$

$$2\partial_{y,h}(\eta_h^n\partial_{y,h})) + \tfrac{1}{2Re}\tfrac{\partial_h(\partial_{y,h}P_h^{n+1,k})}{\partial_h v_h^{n+1,k}} - \tfrac{1}{4Re}\tfrac{\partial_h(\partial_{y,h}(\lambda_h^{n+1,k}(\partial_{y,h}\phi_h^n)^2))+\partial_{x,h}(\lambda_h^{n+1,k}\partial_{x,h}\phi_h^n\partial_{y,h}\phi_h^n)}{\partial v_h^{n+1,k}} ,$$

$$A_{23} = -\tfrac{1}{4Re}(\mu_h^{n+1,k}\partial_{y,h} + \tfrac{\partial\mu_h^{n+1,k}}{\partial\phi_h^{n+1,k}}\partial_{y,h}\phi_h^{n+1,k} + \mu_h^n\partial_{y,h} + \tfrac{\partial\mu_h^{n+1,k}}{\partial\phi_h^{n+1,k}}\partial_{y,h}\phi_h^n) ,$$

$$A_{31} = \tfrac{1}{4}\partial_x(\phi_h^{n+1,k} + \phi_h^n) ,$$

$$A_{32} = \tfrac{1}{4}\partial_y(\phi_h^{n+1,k} + \phi_h^n) ,$$

$$A_{33} = \tfrac{1}{4}((u_h^{n+1,k} + u_h^n)\partial_{x,h} + (v_h^{n+1,k} + v_h^n)\partial_{y,h}) + \mathcal{M}\tfrac{\partial\mu_h^{n+1,k}}{\partial\phi_h^{n+1,k}} .$$

Using Gaussian elimination, the left side of the above matrix system can be transformed as follows:

(4.17)
$$\begin{pmatrix} I - \Delta tA_{11} & \Delta tA_{12} & \Delta tA_{13} \\ 0 & I - \Delta tA_{22} - (\Delta t)^2(I - \Delta tA_{11})^{-1}A_{21}A_{12} & \Delta tA_{23} - (\Delta t)^2(I - \Delta tA_{11})^{-1}A_{21}A_{13} \\ 0 & 0 & A'_{33} \end{pmatrix},$$

where $A'_{33} = I - \Delta tA_{33} - (\Delta t)^2(I - \Delta tA_{22} - (\Delta t)^2(I - \Delta tA_{11})^{-1}A_{21}A_{12})^{-1}A_{32}A_{23}$. C, C' are constant matrices. When Δt is small enough, $I - \Delta tA_{ii}(i = 1, 2, 3)$ is invertible. Thus the given matrix is invertible; we can obtain the unique solution of $(\mathbf{u}_h^{n+1,k+1}, \phi_h^{n+1,k+1})$ with given boundary condition, which means (4.13) is uniquely solvable. ∎

5. Simulation results. Numerical simulations using the model introduced in the paper are presented in this section. The first example is used to illustrate the convergence and energy stability of the proposed numerical scheme. Then feasibility of the proposed model and the model simulation scheme for studying vesicle motion and shape transformation are assessed by cell tank treading and tumbling tests. The last simulation is devoted to studying effects of mechanical and geometric properties of a vesicle on its deformability when it passes through a narrow channel.

5.1. Convergence study. The initial condition of the convergence test is set to be a 2D tear-shaped vesicle in a closed cube with intercellular and extracellular fluid velocity being 0. The initial conditions are

(5.1)
$$\phi_0(x) = \begin{cases} -\tanh[(15(y - 0.185)(y - 0.065) - x + 0.125)/\sqrt{2}\varepsilon], & x < 0.125 \\ -\tanh[(\sqrt{(x - 0.125)^2 + (y - 0.125)^2} - 0.06)/\sqrt{2}\varepsilon], & x >= 0.125, \end{cases}$$
$$\mathbf{u}_0 = (0, 0).$$

Thanks to the bending force of the cell membrane, the shape of the vesicle gradually transforms into a perfect circle to minimize the total energy (see Figure 1). The parameter values used for this simulation are chosen as follows: $Re = 2 \times 10^{-4}$, $\mathcal{M} = 5 \times 10^{-5}$, $\kappa_B = 8 \times 10^{-1}$, $\epsilon = 2.5 \times 10^{-2}$, $\mathcal{M}_v = 20$, $\mathcal{M}_s = 2$, $\xi = 1.6 \times 10^5$, $\kappa = 8 \times 10^{-10}$, $l_s = 5 \times 10^{-3}$.

In the simulations, the numerical solution computed with a mesh size $h = 1/240$ is treated as the reference solution or "the true solution." As shown in Table 1, our scheme is second-order accurate in space.

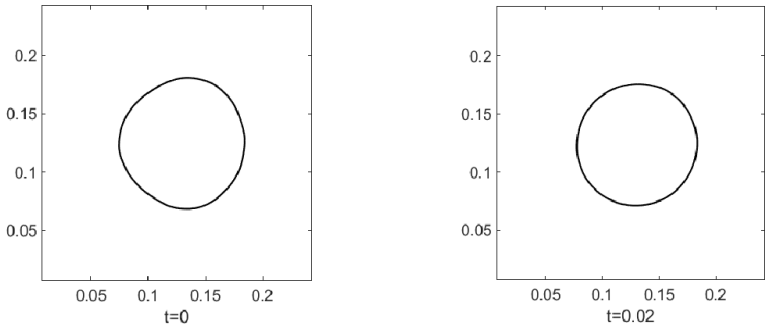

449 FIG. 1. *Relaxation of a tear-shaped vesicle.*

450 TABLE 1
451 *L^2 norm of the error and convergence rate for velocity $\mathbf{u} = (u_x, u_y)$, phase-field function ϕ, at*
452 *time $t = 0.02$ with both intercellular and extracellular fluid viscosity being 1.*

Spatial mesh size h	P2 element					
	Err(u_x)	Convergence rate(u_x)	Err(u_y)	Convergence rate(u_y)	Err(ϕ)	Convergence rate(ϕ)
1/47	1.3e-1		1.5e-1		1.4e-2	
1/71	8.3e-2	1.15	7.6e-2	1.71	6.1e-3	1.97
1/107	3.8e-2	1.94	3.7e-2	1.83	2.3e-3	2.45
1/160	1.5e-2	2.35	1.3e-2	2.59	5.7e-4	3.42

458 TABLE 2
459 *L^2 norm of the error and convergence rate for velocity $\mathbf{u} = (u_x, u_y)$, phase-field function ϕ, at*
460 *time $t = 0.05$ with both intercellular and extracellular fluid viscosities being 1.*

Time step Δt	P2 element					
	Err(u_x)	Convergence rate(u_x)	Err(u_y)	Convergence rate(u_y)	Err(ϕ)	Convergence rate(ϕ)
0.025	-		-		-	
0.0125	8.12e-6		8.13e-6		9.92e-6	
0.00625	2.90e-6	1.49	2.97e-6	1.45	2.42e-6	2.04
0.003125	1.03e-6	1.48	1.07e-6	1.48	5.98e-7	2.01
0.0015625	2.53e-7	2.03	2.60e-7	2.03	1.49e-7	2.01

464 The time convergence rate of the scheme is obtained by comparing the numerical
465 errors calculated using each pair of successively reduced time step sizes. The purpose
466 of doing so is to eliminate the influence from the error of the reference solution which
467 is also a numerical result. Larger Reynolds number Re and interface thickness ϵ and a
468 smoother initial profile of the interface are applied to ensure that the convergence rate
469 is not affected by any sharp changes in the phase-field label function $\phi(\boldsymbol{x})$. Results in
470 Table 2 confirm that our scheme is also second-order accurate in time.

471 *Remark* 5.1. During the convergence test, we mainly focus on the convergence
472 rates of the velocity and the phase-field function. The local inextensibility is neglected,
473 and only the global area and volume constraints are taken into consideration.

474 Finally, the energy law (Theorem 4.1) and conservation of mass and surface area of
475 vesicles are tested by simulating the relaxation of a bent vesicle. The vesicle gradually
476 evolves back to its equilibrium biconcave shape. Figure 2 shows the snapshots of the
477 vesicle profile at different times $t = 0, 0.25, 0.5$, and 1.25. The parameter values used
478 here are as follows:

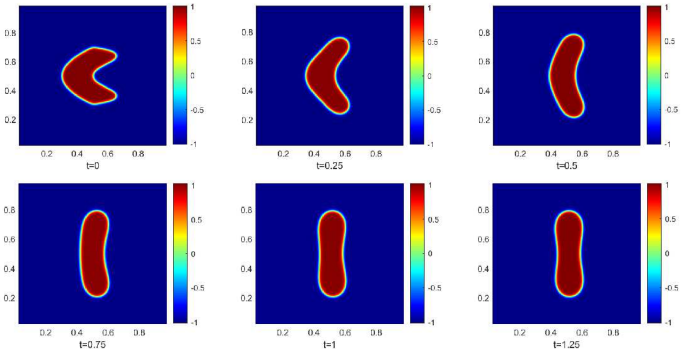

FIG. 2. *Relaxation of a bent vesicle. The fluid viscosities are* 1 *and* 50 *for intercellular and extracellular fluids, respectively.*

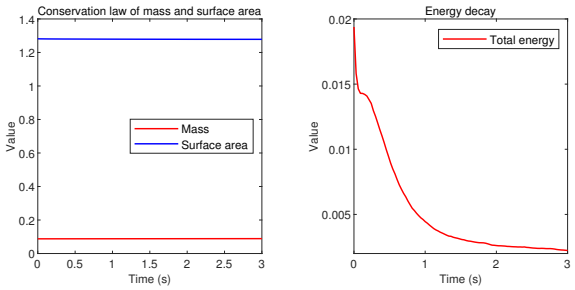

FIG. 3. *The test case of relaxation of a bent vesicle. Left: Change of mass and surface area vs. time. Right: Change of discrete energy vs. time.*

$Re = 2 \times 10^{-4}$, $\mathcal{M} = 2.5 \times 10^{-3}$, $\kappa_B = 2$, $\epsilon = 7.5 \times 10^{-3}$, $\mathcal{M}_v = 20$, $\mathcal{M}_s = 2$, $\xi = 7.1 \times 10^4$, $\kappa = 2 \times 10^{-10}$, $l_s = 0.5$.

The initial conditions are

(5.2)
$$\phi_0(x) = \begin{cases} -tanh[(5(y-0.7)(y-0.3) - x + 0.5)/\sqrt{2}\varepsilon], & x < 0.5 \\ -tanh[(400(y-0.7)(y-0.3)(y-0.5)^2 + x - 0.5)/\sqrt{2}\varepsilon], & x >= 0.5, \end{cases}$$
$$\mathbf{u}_0 = (0, 0).$$

The changes of vesicle mass and surface area and the change of total discrete energy of this test case computed by the scheme (3.1)–(3.2) are shown in Figure 3. It is evident that the vesicle mass and surface area are almost perfectly preserved, and the total energy decays over the course of time as expected.

5.2. Vesicle-wall interaction. This example is used to investigate the effect of the contact line model used for describing vesicle-wall interaction. As shown in Figure 4, a vesicle is initially placed at a location with a pointwise vesicle-wall contact, and a shear flow from left to right is introduced to the system. The parameter values of this simulation are listed as follows:

$Re = 2 \times 10^{-4}, \mathcal{M} = 1.5 \times 10^{-3}, \kappa_B = 0.1, \varepsilon = 0.03, \mathcal{M}_v = 200, \mathcal{M}_s = 2 \times 10^5, \xi = 10^4, \kappa = 1 \times 10^{-10}, \alpha_w = 80, l_s = 0.5$. θ_s is set to be 85° (or 180°) for different interactions between the vesicle and the vessel wall.

Remark 5.2. As can be seen in Figure 4, when the contact angle is 180° high, the cell is carried away by the flow due to an absence of "attraction" between the cell

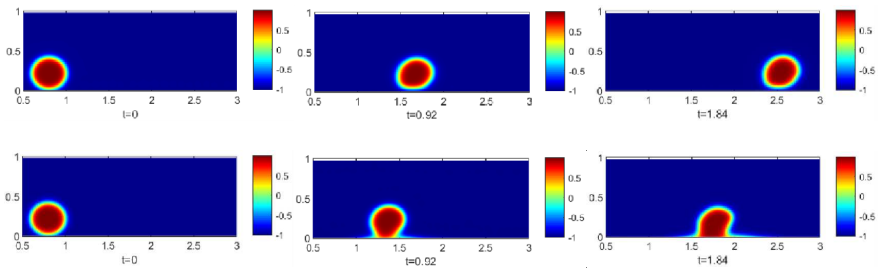

FIG. 4. *The top three pictures show the result of no wetting force modeled using a contact angle* 180°. *The bottom three pictures show the result of an existing cell-wall wetting condition modeled using a contact angle* 85°.

and the wall by a wetting force which is introduced by the contact line model. When the contact angle is significantly lower, say 85°, the vesicle membrane is torn apart at the vesicle-wall contact location due to the existence of a wetting force. We point out that the simulation using an 85° contact angle is not biologically relevant. This shows the limitation of our current model based only on hydrophobicity in considering interaction. The idea of modeling cell-wall adhesion by forming ligand-receptor bonds from [18] could be a good way to model the adhesion force by introducing a wall phase and its interacting potential with the vesicle phase. We will thus use a significantly higher contact angle, i.e., $\theta_s = 180°$, in the rest of the simulations presented in the paper.

5.3. Tank treading and tumbling. The vesicle motion in a Couette flow changes with respect to the ratio of the viscosities η_{in} and η_{out} of intracellular and extracellular fluids [32, 4, 16, 24]. When this viscosity ratio is small, the vesicle is prone to move in the tank treading mode, while the tumbling mode is preferred when the viscosity ratio is large. The parameter values utilized for this vesicle motion simulation are set as follows:

$Re = 2\times10^{-4}$, $\delta_\epsilon = |\nabla\phi^n|^2$, $\mathcal{M} = 10^{-3}$, $\kappa_B = 5\times10^{-3}$, $\epsilon = 7.5\times10^{-3}$, $\mathcal{M}_v = 20$, $\mathcal{M}_s = 200$, $\xi = 1.78\times10^{7}$, $\kappa = 2\times10^{-12}$, $l_s = 0.2$.

The upper and bottom walls of the domain are set to move in opposite directions horizontally with velocities -20 and 20, respectively. The simulation domain is 2×1, and the initial shape of the vesicle is chosen to be an ellipse with eccentricity $\sqrt{3}$. The ratios of viscosities of the intracellular and extracellular fluids are set to be $1:1$ and $1:500$, respectively. Figure 5 shows the interfaces of tank treading vesicle (low viscosity ratio case) and tumbling vesicle (high viscosity ratio case) and corresponding fluid velocity fields at different times, respectively. A point on the interface (black solid) is tracked to illustrate these two different types of motion. For the tank treading motion, the angle between the long axis of the vesicle and the horizontal axis is fixed when the vesicle is at equilibrium, but the tracer point rotates in a counterclockwise direction along the membrane. For the tumbling motion, the vesicle keeps rotating, and the tracer point does not move with respect to the membrane shape.

Remark 5.3. Tracking of the marker point (the black solid dot) is done by the following steps:

1. Determine a marker point P that is located on the interface with coordinate (x, y).
2. Compute the velocity $\mathbf{u}(P) = (u_x(P), u_y(P))$ of the marker point by interpolation.

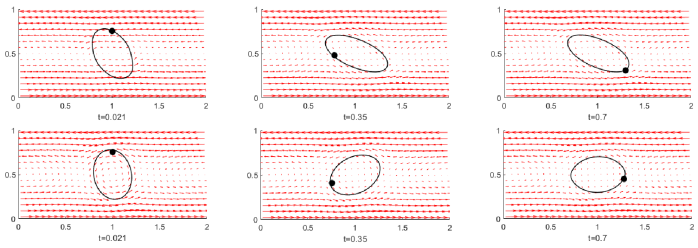

FIG. 5. *Top: Tank treading with viscosity ratio* $1:1$. *The orientation of the vesicle and the velocity field are kept stable when the system comes to equilibrium. Bottom: Tumbling with viscosity ratio* $1:500$. *The vesicle keeps rotating in the flow. Position of the tracer point (in black) is fixed with respect to the vesicle membrane.*

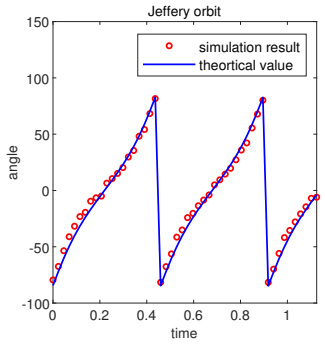

FIG. 6. *Comparison between theoretical and simulation results of the flipping ellipse. The blue line is the angle between the long axis of the ellipse and the horizontal axis predicted by the Jeffery orbit theory, and the red circles are the angle from the simulation.*

3. Update the marker point position at the next time point by $(x+u_x(P)\Delta t, y+u_y(P)\Delta t)$.
4. Go to step 2.

This tracking gives the trajectory of the marker point.

Next, the simulation result of tumbling motion of a rigid ellipse is compared with the theoretical solution obtained using Jeffery's orbit theory [28]. Specifically, the angle between the long axis of the ellipse and the horizontal axis is compared. As shown in Figure 6, our simulation result is in close agreement with the analytical Jeffery orbit.

Remark 5.4. The long axis of the rigid ellipse during the tumbling motion is determined as follows:

1. Determine the interface location of the ellipse by $\phi = 0$.
2. Find the point on the interface that is farthest away from the center of the vesicle in the upper domain.
3. Match these two points, and the line is considered as the long axis of the ellipse.

Since the ellipse is located at the center of the domain at the initial time point, and the motion of the fluid is centrosymmetric according to the specified boundary condition, it is expected that the center of the ellipse is kept at the center of the domain Ω. Therefore the determination of the long axis of the ellipse based on its geometry character is acceptable.

5.4. Vesicle passing through a narrow fluid channel. Finally, the calibrated model is used to study the effects of mechanical properties of the membrane of the vesicle on its circulating through constricting micro channels [23]. The vesicle shape is described by an ellipse with eccentricity $\sqrt{3}$, and the width of the squeezing section of the narrow channel is 0.3 by default. A pressure drop boundary condition is applied at the inlet (left) and outlet (right) of the domain by setting the pressure on the inlet and outlet to be $P = 50$ and $P = -50$, respectively. The fluid viscosity ratio is set to be $1 : 10$ for extracellular and intracellular fluids, respectively. The other parameters are as follows:

$Re = 2 \times 10^{-4}$, $\delta_\epsilon = 10 \times |\nabla \phi^n|^2$, $\mathcal{M} = 5 \times 10^{-4}$, $\kappa_B = 4 \times 10^{-2}$, $\epsilon = 7.5 \times 10^{-3}$, $\mathcal{M}_v = 20$, $\mathcal{M}_s = 100$, $\xi = 7.1 \times 10^4$, $\kappa = 4 \times 10^{-11}$, $l_s = 5 \times 10^{-3}$.

The effect of the local inextensibility of the vesicle membrane is assessed by comparing vesicle simulations with and without using the local inextensibility constraint $\mathcal{P} : \nabla \mathbf{u} = 0$ in the model. Snapshots of these simulations at different times are shown in Figure 7. They illustrate that a vesicle modeled without using the local inextensibility can pass through the channel by introducing large extension and deformation of its body with a relatively small value of global inextensibility coefficient $\mathcal{M}_s$, while a vesicle modeled with the local inextensibility hardly exhibits large extension and deformation of its body and blocks the channel. This is also confirmed by Figure 8. It shows that under otherwise identical conditions, the total arc length of the membrane of the vesicle modeled without the local inextensibility increases significantly when it passes through the channel, and the vesicle with the local inextensibility preserves its membrane arc length well during the course of the simulation.

Although the total arc length of a vesicle without the local inextensibility and with a very large $\mathcal{M}_s$ value could maintain almost unchanged as shown in Figures 7(c) and 8, the morphological changes of vesicles with and without the local inextensibility are drastically different. For the vesicles modeled without the local inextensibility, Figure 9(b) and (c) illustrates that the vesicle membranes are stretched (red) or compressed (blue) everywhere, even though the total arc length of the vesicle modeled using a large modulus $\mathcal{M}_s$ value could be preserved, and the vesicle forms a blockage. For the vesicle modeled with the local inextensibility, Figure 9(c) confirms that there is almost no local extension or compression of the membrane, which is consistent with experimental observations. All simulations described below use the local inextensibility.

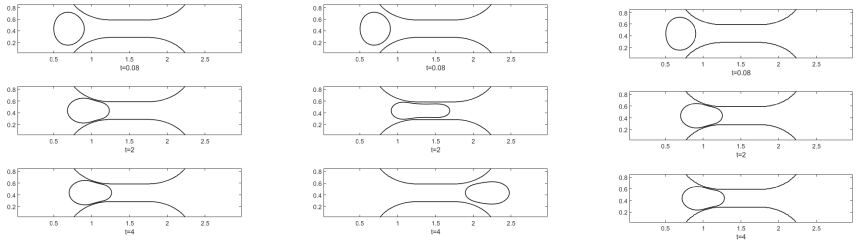

(a) (b) (c)

FIG. 7. *Snapshots of vesicles passing through a narrowed channel with different surface area constraints at times* $t = 0.08, 2,$ *and* 4*, respectively.* (a) $\mathcal{M}_s = 100$ *with the local inextensibility;* (b) $\mathcal{M}_s = 100$ *without the local inextensibility;* (c) $\mathcal{M}_s = 20000$ *without the local inextensibility. The curves on the top and bottom ceiling are the wall boundary of the narrowed channel.*

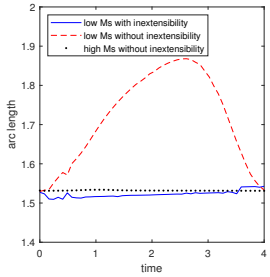

606 FIG. 8. *Total arc length of vesicle membrane with the local inextensibility (blue line) and the*
607 *total arc lengths of vesicle membranes with low* (100) *(red dashed line) and high* (20000) *(black*
608 *point)* $\mathcal{M}_s$ *and no local inextensibility, respectively, during vesicles passing through the constriction*
609 *of the micro channel with otherwise identical parameter values and settings.*

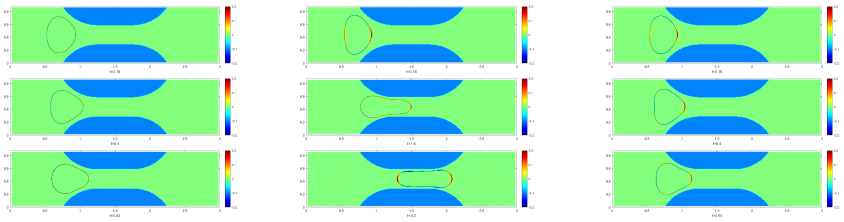

(a) (b) (c)

610 FIG. 9. *Effects of the local inextensibility* $\mathcal{P} : \nabla \mathbf{u} = 0$. *Snapshots of membrane forces of vesicles:*
611 (a) $\mathcal{M}_s = 100$ *with the local inextensibility,* (b) $\mathcal{M}_s = 100$ *without the local inextensibility, and* (c)
612 $\mathcal{M}_s = 20000$ *without the local inextensibility.*

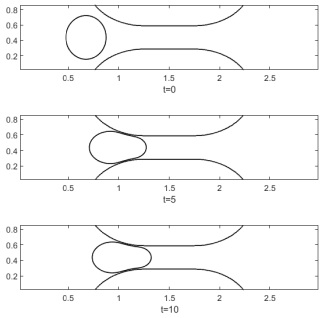

613 FIG. 10. *Side view of a vesicle with surface-volume ratio* 1.5 : 1 *at different times.*

614 Both experiments and clinical reports have shown that the cell bending modu-
615 lus and surface-volume ratio play important roles in determining the deformability
616 of vesicles, especially when they pass through narrow channels [55, 38, 49]. The lat-
617 est results reveal that a moderate decrease in the surface-volume ratio has a more
618 significant effect than varying the cell bending stiffness. This surface-volume ratio
619 effect is tested by increasing the ratio value slightly from 1.5 : 1 to 2 : 1. Results in
620 Figures 10 and 11 confirm that the more rounded vesicles are much harder to pass
621 through the narrow channel and can easily form a blockage. This is consistent with
622 the experimental observations.

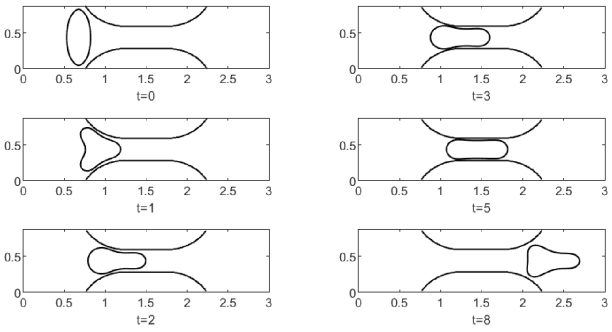

627 FIG. 11. *Side view of a vesicle with surface-volume ratio* $2:1$ *at different times.*

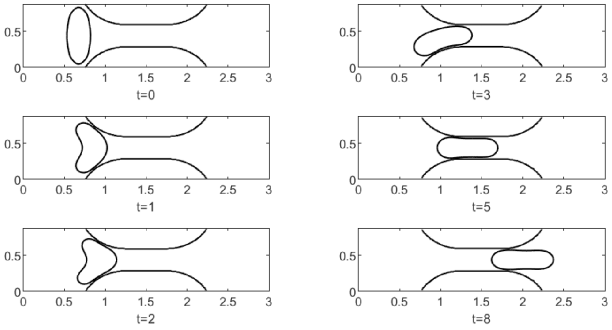

628 FIG. 12. *Side view of a vesicle with large bending modulus* $\kappa_B = 4 \times 10^{-1}$ *and surface-volume*
629 *ratio* $2:1$ *at different times.*

623 The effect of the bending modulus is assessed by increasing its value 10 times.
624 The surface-volume ratio of the vesicle is $2:1$ in this test. Figure 11 illustrates that
625 this more rigid vesicle can also pass through the same size channel but exhibits very
626 different shape transformation.

630 **6. Conclusion.** In this paper, an energy variational method is used to derive
631 a thermodynamically consistent phase-field model for simulating vesicle motion and
632 deformation under flow conditions. Corresponding Allen–Cahn GNBCs accounting
633 for the vesicle-wall (or fluid-structure) interaction are also proposed by introducing
634 the proper boundary dissipation and vesicle-wall interaction energy.
635 Then an efficient scheme using C^0 finite element spatial discretization and the
636 midpoint temporal discretization is proposed to solve the obtained model equations.
637 Thanks to the midpoint temporal discretization, the obtained numerical scheme is
638 unconditionally energy stable. The numerical experiments confirm that this scheme is
639 second-order accurate in both space and time. Simulations of the vesicle tank treading
640 and tumbling motions reproduce experimental observations. And the flipping ellipse
641 simulation agrees with the analytical solution well. Finally, the model is used to
642 investigate how vesicles' mechanical properties affect the vesicles' capability to pass
643 through narrow channels. It is shown that whether a vesicle can pass through a
644 narrow channel is largely determined by the surface-volume ratio of the vesicle, which
645 is consistent with in vitro experiments.

Our model can be used to study the impaired dynamics of red blood cells due to altered mechanical properties of red blood cell membranes in sickle cell disease [3] and in diabetes [36]. Combining with the restricted diffusion model [46], our model can be generalized to model the mass transfer through a semipermeable membrane, for example, oxygen delivering [57].

There are limitations in our model if we need to consider an adhesion based on the ligand-receptor binding. When the static contact angle is lower than 180°, the vesicle is torn apart due to the wetting effect. In [18], the authors proposed an adhesion model by introducing a new phase label for vascular wall and an adhesion energy functional using labels of wall phase and cell. In the future, we will combine the adhesion model with the contact line model and more realistic submodels for cell-wall and cell-cell interactions to model the cell aggregation [63, 64], cell crawling, and invasion problems [51, 9].

REFERENCES

[1] S. Aland, S. Egerer, J. Lowengrub, and A. Voigt, *Diffuse interface models of locally inextensible vesicles in a viscous fluid*, J. Comput. Phys., 277 (2014), pp. 32–47.

[2] J. E. Aslan, A. Itakura, J. M. Gertz, and O. J. McCarty, *Platelet shape change and spreading*, in Platelets and Megakaryocytes, Springer, Cham, 2012, pp. 91–100.

[3] G. A. Barabino, M. O. Platt, and D. K. Kaul, *Sickle cell biomechanics*, Ann. Rev. Biomed. Eng., 12 (2010), pp. 345–367.

[4] H. Basu, A. K. Dharmadhikari, J. A. Dharmadhikari, S. Sharma, and D. Mathur, *Tank treading of optically trapped red blood cells in shear flow*, Biophys. J., 101 (2011), pp. 1604–1612.

[5] J. Beaucourt, F. Rioual, T. Séon, T. Biben, and C. Misbah, *Steady to unsteady dynamics of a vesicle in a flow*, Phys. Rev. E, 69 (2004), 011906.

[6] A. Bonito, R. H. Nochetto, and M. S. Pauletti, *Parametric FEM for geometric biomembranes*, J. Comput. Phys., 229 (2010), pp. 3171–3188.

[7] R. Chen, G. Ji, X. Yang, and H. Zhang, *Decoupled energy stable schemes for phase-field vesicle membrane model*, J. Comput. Phys., 302 (2015), pp. 509–523.

[8] P. G. Ciarlet, *Introduction to Linear Shell Theory*, Elsevier, New York, 1998.

[9] Y. Connor, Y. Tekleab, S. Tekleab, S. Nandakumar, D. Bharat, and S. Sengupta, *A mathematical model of tumor-endothelial interactions in a 3d co-culture*, Sci. Rep., 9 (2019), pp. 1–14.

[10] Q. Du, C. Liu, R. Ryham, and X. Wang, *Modeling the spontaneous curvature effects in static cell membrane deformations by a phase field formulation*, Comm. Pure Appl. Anal., 4 (2005), p. 537.

[11] Q. Du, C. Liu, R. Ryham, and X. Wang, *A phase field formulation of the Willmore problem*, Nonlinearity, 18 (2005), p. 1249.

[12] Q. Du, C. Liu, R. Ryham, and X. Wang, *Energetic variational approaches in modeling vesicle and fluid interactions*, Phys. D, 238 (2009), pp. 923–930.

[13] Q. Du, C. Liu, and X. Wang, *A phase field approach in the numerical study of the elastic bending energy for vesicle membranes*, J. Comput. Phys., 198 (2004), pp. 450–468.

[14] Q. Du and J. Zhang, *Adaptive finite element method for a phase field bending elasticity model of vesicle membrane deformations*, SIAM J. Sci. Comput., 30 (2008), pp. 1634–1657.

[15] B. Eisenberg, Y. Hyon, and C. Liu, *Energy variational analysis of ions in water and channels: Field theory for primitive models of complex ionic fluids*, J. Chem. Phys., 133 (2010), 104104.

[16] T. M. Fischer, *Shape memory of human red blood cells*, Biophys. J., 86 (2004), pp. 3304–3313.

[17] C. G and P. RL., *Techniques to evaluate erythrocyte deformability in diabetes mellitus*, Acta Diabetol., 41 (2004), pp. 99–103.

[18] R. Gu, X. Wang, and M. Gunzburger, *Simulating vesicle–substrate adhesion using two phase field functions*, J. Comput. Phys., 275 (2014), pp. 626–641.

[19] R. Gu, X. Wang, and M. Gunzburger, *A two phase field model for tracking vesicle–vesicle adhesion*, J. Math. Biol., 73 (2016), pp. 1293–1319.

[20] F. Guillén-González and G. Tierra, *Unconditionally energy stable numerical schemes for phase-field vesicle membrane model*, J. Comput. Phys., 354 (2018), pp. 67–85.

[21] Z. Guo and P. Lin, *A thermodynamically consistent phase-field model for two-phase flows with thermocapillary effects*, J. Fluid Mech., 766 (2015), pp. 226–271.
[22] Z. Guo, P. Lin, and J. S. Lowengrub, *A numerical method for the quasi-incompressible Cahn–Hilliard–Navier–Stokes equations for variable density flows with a discrete energy law*, J. Comput. Phys., 276 (2014), pp. 486–507.
[23] Y. Han, H. Lin, M. Ding, R. Li, and T. Shi, *Flow-induced translocation of vesicles through a narrow pore*, Soft Matter, 15 (2019), pp. 3307–3314.
[24] W. Hao, Z. Xu, C. Liu, and G. Lin, *A fictitious domain method with a hybrid cell model for simulating motion of cells in fluid flow*, J. Comput. Phys., 280 (2015), pp. 345–362.
[25] D. Hu, P. Zhang, and E. Weinan, *Continuum theory of a moving membrane*, Phys. Rev. E, 75 (2007), 041605.
[26] W.-F. Hu, M.-C. Lai, Y. Seol, and Y.-N. Young, *Vesicle electrohydrodynamic simulations by coupling immersed boundary and immersed interface method*, J. Comput. Phys., 317 (2016), pp. 66–81.
[27] J. Hua, P. Lin, C. Liu, and Q. Wang, *Energy law preserving c0 finite element schemes for phase field models in two-phase flow computations*, J. Comput. Phys., 230 (2011), pp. 7115–7131.
[28] G. B. Jeffery, *The motion of ellipsoidal particles immersed in a viscous fluid*, Proc. A, 102 (1922), pp. 161–179.
[29] J. T. Jenkins, *The equations of mechanical equilibrium of a model membrane*, SIAM J. Appl. Math., 32 (1977), pp. 755–764.
[30] Y. Kim and M.-C. Lai, *Simulating the dynamics of inextensible vesicles by the penalty immersed boundary method*, J. Comput. Phys., 229 (2010), pp. 4840–4853.
[31] E. M. Kolahdouz and D. Salac, *A numerical model for the trans-membrane voltage of vesicles*, Appl. Math. Lett., 39 (2015), pp. 7–12.
[32] A. Laadhari, P. Saramito, and C. Misbah, *Vesicle tumbling inhibited by inertia*, Phys. Fluids, 24 (2012), 031901.
[33] Z. Li, X. Bian, Y.-H. Tang, and G. E. Karniadakis, *A dissipative particle dynamics method for arbitrarily complex geometries*, J. Comput. Phys., 355 (2018), pp. 534–547.
[34] X. Liu, F. Song, and C. Xu, *An efficient spectral method for the inextensible immersed interface in incompressible flows*, Commun. Comput. Phys., 25 (2019), pp. 1071–1096.
[35] J. S. Lowengrub, A. Rätz, and A. Voigt, *Phase-field modeling of the dynamics of multicomponent vesicles: Spinodal decomposition, coarsening, budding, and fission*, Phys. Rev. E, 79 (2009), 031926.
[36] R. Malka, D. M. Nathan, and J. M. Higgins, *Mechanistic modeling of hemoglobin glycation and red blood cell kinetics enables personalized diabetes monitoring*, Sci. Transl. Med., 8 (2016), 359ra130.
[37] W. Marth, S. Aland, and A. Voigt, *Margination of white blood cells: a computational approach by a hydrodynamic phase field model*, J. Fluid Mech., 790 (2016), pp. 389–406.
[38] A. Namvar, A. J. Blanch, M. W. Dixon, O. M. Carmo, B. Liu, S. Tiash, O. Looker, D. Andrew, L.-J. Chan, W.-H. Tham, P. V. S. Lee, V. Rajagopal, and L. Tilley, *Surface area-to-volume ratio, not cellular viscoelasticity, is the major determinant of red blood cell traversal through small channels*, Cell. Microbiol., 23 (2021), e13270.
[39] K. C. Ong and M.-C. Lai, *An immersed boundary projection method for simulating the inextensible vesicle dynamics*, J. Comput. Phys., 408 (2020), 109277.
[40] I. V. Pivkin and G. E. Karniadakis, *Accurate coarse-grained modeling of red blood cells*, Phys. Rev. Lett., 101 (2008), 118105.
[41] I. V. Pivkin, P. D. Richardson, and G. E. Karniadakis, *Effect of red blood cells on platelet aggregation*, IEEE Eng. Med. Biol. Mag., 28 (2009), pp. 32–37.
[42] J. Pöschl, C. Leray, P. Ruef, J. Cazenave, and O. Linderkamp, *Endotoxin binding to erythrocyte membrane and erythrocyte deformability in human sepsis and in vitro*, Crit. Care Med., 31 (2003), pp. 924–928.
[43] T. Qian, X.-P. Wang, and P. Sheng, *Molecular hydrodynamics of the moving contact line in two-phase immersible flows*, Commun. Comput. Phys., 1 (2006), pp. 1–52.
[44] T. Qian, X.-P. Wang, and P. Sheng, *A variational approach to moving contact line hydrodynamics*, J. Fluid Mech., 564 (2006), p. 333, https://doi.org/10.1017/S0022112006001935.
[45] T. Qian, X.-P. Wang, and P. Sheng, *A variational approach to moving contact line hydrodynamics*, J. Fluid Mech., 564 (2006), pp. 333–360.
[46] Y. Qin, H. Huang, Y. Zhu, C. Liu, and S. Xu, *A Phase Field Model for Mass Transport with Semi-Permeable Interfaces*, arXiv preprint, arXiv:2103.06430 [math.NA], 2021.
[47] W. Ren and W. E, *Heterogeneous multiscale method for the modeling of complex fluids and micro-fluidics*, J. Comput. Phys., 204 (2005), pp. 1–26, https://doi.org/10.1016/j.jcp.2004.10.001.

765 [48] W. Ren and W. E, *Boundary conditions for the moving contact line problem*, Phys. Fluids,
766 19 (2007), 022101.
767 [49] C. Renoux, M. Faivre, A. Bessaa, L. Da Costa, P. Joly, A. Gauthier, and P. Connes,
768 *Impact of surface-area-to-volume ratio, internal viscosity and membrane viscoelasticity on*
769 *red blood cell deformability measured in isotonic condition*, Sci. Rep., 9 (2019), pp. 1–7.
770 [50] D. Salac and M. Miksis, *A level set projection model of lipid vesicles in general flows*, J.
771 Comput. Phys., 230 (2011), pp. 8192–8215.
772 [51] N. J. Savill and P. Hogeweg, *Modelling morphogenesis: From single cells to crawling slugs*,
773 J. Theoret. Biol., 184 (1997), pp. 229–235.
774 [52] Y. Seol, W.-F. Hu, Y. Kim, and M.-C. Lai, *An immersed boundary method for simulating*
775 *vesicle dynamics in three dimensions*, J. Comput. Phys., 322 (2016), pp. 125–141.
776 [53] L. Shen, H. Huang, P. Lin, Z. Song, and S. Xu, *An energy stable $C0$ finite element scheme*
777 *for a quasi-incompressible phase-field model of moving contact line with variable density*,
778 J. Comput. Phys., 405 (2020), 109179.
779 [54] E.-K. Shin, H. Park, J.-Y. Noh, K.-M. Lim, and J.-H. Chung, *Platelet shape changes and*
780 *cytoskeleton dynamics as novel therapeutic targets for anti-thrombotic drugs*, Biomol. Ther-
781 apeutics, 25 (2017), p. 223.
782 [55] S. Takagi, T. Yamada, X. Gong, and Y. Matsumoto, *The deformation of a vesicle in a*
783 *linear shear flow*, J. Applied Mech., 76 (2009), 021207.
784 [56] N. Takeishi, H. Ito, M. Kaneko, and S. Wada, *Deformation of a red blood cell in a narrow*
785 *rectangular microchannel*, Micromachines, 10 (2019), p. 199.
786 [57] X. Wang, X. Gong, K. Sugiyama, S. Takagi, and H. Huang, *An immersed boundary method*
787 *for mass transfer through porous biomembranes under large deformations*, J. Comput.
788 Phys., 413 (2020), 109444.
789 [58] H. Wu and X. Xu, *Strong solutions, global regularity, and stability of a hydrodynamic system*
790 *modeling vesicle and fluid interactions*, SIAM J. Math. Anal., 45 (2013), pp. 181–214.
791 [59] T. Wu and J. J. Feng, *Simulation of malaria-infected red blood cells in microfluidic channels:*
792 *Passage and blockage*, Biomicrofluidics, 7 (2013), 044115.
793 [60] J.-J. Xu, Z. Li, J. Lowengrub, and H. Zhao, *A level-set method for interfacial flows with*
794 *surfactant*, J. Comput. Phys., 212 (2006), pp. 590–616, https://doi.org/10.1016/j.jcp.2005.
795 07.016.
796 [61] J.-J. Xu and W. Ren, *A level-set method for two-phase flows with moving contact line and*
797 *insoluble surfactant*, J. Comput. Phys., 263 (2014), pp. 71–90, https://doi.org/10.1016/j.
798 jcp.2014.01.012.
799 [62] S. Xu, P. Sheng, and C. Liu, *An energetic variational approach for ion transport*, Commun.
800 Math. Sci., 12 (2014), pp. 779–789.
801 [63] S. Xu, Z. Xu, O. V. Kim, R. I. Litvinov, J. W. Weisel, and M. Alber, *Model predictions*
802 *of deformation, embolization and permeability of partially obstructive blood clots under*
803 *variable shear flow*, J. Roy. Soc., Interface, 14 (2017), 20170441, https://doi.org/10.1098/
804 rsif.2017.0441.
805 [64] Z. Xu, N. Chen, M. M. Kamocka, E. D. Rosen, and M. Alber, *A multiscale model of*
806 *thrombus development*, J. Roy. Soc. Interface, 5 (2008), pp. 705–722.
807 [65] X. Yang, J. Zhao, Q. Wang, and J. Shen, *Numerical approximations for a three-component*
808 *Cahn–Hilliard phase-field model based on the invariant energy quadratization method*,
809 Math. Models Methods Appl. Sci., 27 (2017), pp. 1993–2030.